universität wien

MASTERARBEIT / MASTER'S THESIS

Titel der Masterarbeit / Title of the Master's Thesis

„Electrospray Generation of Monomobile Mobility Standards with three Aerosol Neutralizers “

verfasst von / submitted by

Iris Brodacz, BA BSc

angestrebter akademischer Grad / in partial fulfilment of the requirements for the degree of

Master Of Science (MSc)

Wien, 2017 / Vienna, 2017

Studienkennzahl lt. Studienblatt / degree programme code as it appears on the student record sheet:	A 066 876
Studienrichtung lt. Studienblatt / degree programme as it appears on the student record sheet:	Masterstudium Physik
Betreut von / Supervisor:	Dr. Gerhard Steiner

Acknowledgements

I would like to thank especially

- Dr. Gerhard Steiner for supervising my master thesis, for his dedicated support, his scientific inputs, enthusiasm and patience
- the entire aerosol group at the faculty of physics for so many interesting conversations

I also want to thank my mother for her support and patience, Thomas and my sister for taking the time to proofread this thesis, as well as all of my friends who had to listen to me talking about tetraheptyl ammonium bromide. [1]

[1] Zaldrīzes buzdari iksos daor

1 Abstract

The goal of this thesis is to extend the applicability of tetra-alkyl ammonium halides (TAAH) used as electrical mobility standards for instrument calibration and performance evaluation. In an electrical mobility spectrum, tetra-alkyl ammonium halides produce a unique series of sharp peaks, with each peak corresponding to one monomobile cluster species. For the electrical mobility measurement, an electrospray ion source is used as the particle generator, a high resolution differential mobility analyzer for the classification of the molecular clusters, and a Faraday cup electrometer as particle detector. Since the electrical mobility is indirectly proportional to the particle's diameter and directly proportional to the particle's charging state, larger multiply charged TAAH i-mer clusters have the same electrical mobility as smaller singly charged ones. For this reason only cluster species with a diameter $D_p < 2$ nm can so far easily be unambiguously identified. This thesis addresses the issue by using three aerosol neutralizers for the purpose of charge reduction. Two of them are bipolar ionizers, based on ionizing radiation from a radionuclide and from a soft X-ray source. A corona neutralizer used as a unipolar ionizer was designed and built for this thesis.

The experimental work demonstrated that the eligibility of the neutralizer is very much dependent on the test substances in use. The custom-built corona ionizer shows high potential in the reduction of multiply charged particles but is still calling for a more thorough evaluation in future studies.

2 Kurzfassung

Das Ziel dieser Arbeit ist es, die Anwendbarkeit von tetra-alkyl Ammonium Halogeniden (TAAH) als elektrische Mobilitätsstandards für die Kalibrierung und zur Leistungsanalyse von Instrumenten zu erweitern. In Mobilitätsspektren erzeugen tetra-alkyl Ammonium Halogenide eine einzigartige Abfolge scharfer Peaks, wobei jeder Peak einer monomobilen Cluster-Spezies entspricht. Für die Messung der elektrischen Mobilität, werden die von einer Elektrospray-Ionenquelle erzeugten molkularen Cluster mit einem hochauflösenden differentiellen Mobilitätsanalysator, klassifiziert und von einem Faraday-Cup-Elektrometer detektiert. Da die elektrische Mobilität indirekt proportional zum Durchmesser und direkt proportional zum Ladezustand des Teilchens ist, haben größere mehrfach geladene TAAH i-mer Cluster die gleiche elektrische Mobilität wie kleinere einzeln geladene Cluster. Aus diesem Grund können bisher nur Cluster-Spezies mit einem Durchmesser $D_p < 2$ nm eindeutig identifiziert werden. Diese Arbeit befasst sich mit dieser Problemstellung indem durch die Verwendung von drei Aerosol-Neutralisatoren versucht wird überschüssige Ladungen zu neutralisieren, um Cluster mit Durchmessern von 3-4 nm sichtbar und zugänglich zu machen. Zwei der Neutralisatoren sind bipolare Ionisatoren, basierend auf ionisierender Strahlung eines Radionuklids und einer Weich-Röntgenquelle. Ein unipolarer Ionisator basierend auf einer Koronaentladung wurde im Zuge dieser Arbeit konzipiert und gebaut. Die Experimente zeigten, dass die Eignung der verschiedenen Neutralisatoren abhängig von der zu untersuchenden Cluster-Spezies ist.

Der speziell angefertigte Korona-Ionisator zeigt ein hohes Potential zur Reduktion von Mehrfachladungen der Teilchen, fordert jedoch eine detaillierte Evaluation in zukünftigen Studien.

Contents

3 Introduction and Motivation

Aerosol sciences is a manifold scientific field of major relevance as it is i.a. concerned with the effects of airborne particles on the earth's radiative balance and their influence on climate change. Furthermore, aerosol particles are also of interest concerning human health hazards associated with air pollution, especially particulate matter and smog. A deeper knowledge about the chemical nature and structure, size distribution and mass/number concentration of the respective aerosol (particles) is crucial to target these pressing issues. Electrical mobility measurements using a differential mobility analyzer (DMA) in combination with a suitable detector like an electrometer or condensation particle counter (CPC) allows the determination of the electrical particle mobility and the according number concentration. In order to gain unambiguous and reproducible measurement results, instrument calibration and evaluation are crucial preconditions (Flagan, 1999; Baron and Willeke, 2001; Kulkarni et al., 2011; Hinds, 1999). For electrical mobility measurements this is generally done by determining the voltage at which the majority of 'test aerosol particles' of a well-known electrical mobility gets measured (Steiner et al., 2010). For a known charge distribution, a particle's electrical mobility equivalent diameter can then be derived from its electrical mobility. There are different possibilities to provide the necessary mobility and size standards. First, by using a tandem DMA setup where the first instrument classifies a monomobile size fraction from a polydisperse aerosol. This fraction is then fed to the instrument that is meant to be calibrated. Second, by using size standards. Following the definition from Liu and Pui (1974), "[w]hen the particle size and concentration are known to a sufficiently high degree of accuracy, these aerosols may be referred to as aerosol standards."(Liu and Pui, 1974, 157) Size standards are also used to study the influence of particle size on instrument performance. The advantage of using aerosol standards rather than monomobile size

fractions lies in the fact that the monomobility of the fraction is dependent on the resolution of the first DMA. Suspensions of polystyrene latex particles (PSL) are very often used as test particles within the size range $D_p > 20$ nm to 1 μm due to their narrow size distribution and spherical shape. To generate the particle in this size range, suspensions are usually atomized. There are a multitude of atomizers which are distinguished by their underlying operating principle. A very important subset of atomizers are nebulizers. Vibrating-orifice aerosol generator and the spinning-disk aerosol generator are two examples for monodisperse atomizers. Research efforts towards even smaller particle sizes in the nanometer region requested new procedures of aerosol generation. One possibility is electrical atomization with an electrospray, which allows the generation of particles with diameters

$D_p \leq 2$ nm (Hinds, 1999; Baron and Willeke, 2001). Good results were achieved by electrospraying solutions of large organic salts, like tetra-alkyl ammonium halides (TAAHs) dissolved in high purity alcohols. Using this technique, it is possible to generate charged molecular clusters and even single molecular ions. The resulting aerosol is not only monomobile but also true monodisperse. TAAH clusters are therefore especially important as aerosol standards for instrument calibration and performance tests in the sub 10 nm range (Ude and Fernández de la Mora, 2005). However, one problem arises: even though the smallest cluster species (monomer, dimer, trimer) with el. mobility equivalent diameters below 2 nm can be determined accurately, higher order i-mers with lower electrical mobilities cannot. The electrical mobility spectrum within this region gets distorted. The individual cluster species cannot be resolved, because larger multiply charged clusters superimpose smaller singly charged ones. This is because the probability for multiple charging increases with increasing particle diameter and because electrical mobility increases with an increasing number of charges (Hinds, 1999). This process can

be avoided by using an aerosol neutralizer, which allows the reduction of charges to one. This work addresses this issue by comparing three different aerosol neutralizers: a radioactive source, a soft X-ray ionizer and a corona neutralizer. The former two are bipolar ionizers, whereas the latter one is a unipolar ionizer. The monomobile molecular clusters of different tetra-alkyl ammonium halide ions are generated using an electrospray ion source and are classified by a high resolution DMA (Steiner et al., 2010). The number concentration of charged clusters exiting the DMA is determined by a Faraday cup electrometer. The idea behind this thesis is to realize higher order cluster species of tetraheptyl ammonium bromide (THABr) and other halides by using a neutralizer, trying to access clusters up to 3-4 nm as calibration standards.

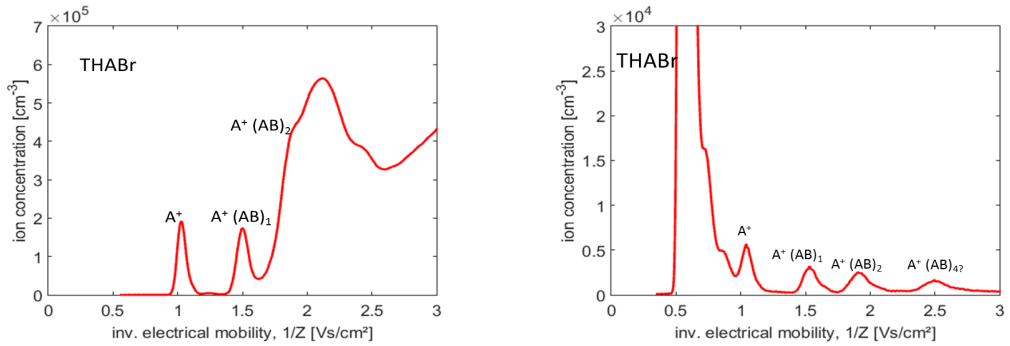

(a) Positive spray: THABr electrical mobility spectrum

(b) Positive THABr electrical mobility spectrum with ^{241}Am

Figure 1: Inverse mobility spectrum of positively charged THABr clusters. On the left hand side without a neutralizer, and on the right hand side with a radioactive source as a bipolar neutralizer.

4 Physical Basis

Chapter 4 is an introductory chapter on the relevant physical basis of this thesis. It is based on the standard textbooks by Hinds (1999), Baron and Willeke (2001), Kulkarni et al. (2011) and Seinfeld and Pandis (2006), with further emphasis on charging theory by Fuchs (1963), going beyond the Boltzmann description of equilibrium charge distribution.

4.1 Linear Particle Motion and Diffusion

It is important to keep in mind that by definition an aerosol is made of liquid and/or solid particles suspended in a carrier gas (Hinds, 1999). Consequently, gas and particle properties, as well as behavior and their interaction are of interest.

Kinetic gas theory

"According to kinetic theory, the temperature, pressure, mean free path, and viscosity of a gas are manifestations of the motion of the gas molecules."(Hinds, 1999, 15) The classical kinetic theory of gases is based on three assumptions: first, gas is made up of many molecules, second, the distance between molecules is large compared to their radii and third, molecules may be considered as rigid spheres. Furthermore, gas molecules move on straight paths, and collisions between them are elastic (Hinds, 1999).

The ideal gas law, see equation (1), connects pressure p, volume V, number of moles n and the absolute temperature T.

R denotes the universal gas constant, its value is dependent on the units used (SI units: $R = 8,314 \frac{\mathrm{J}}{\mathrm{mol \cdot K}}$). The ideal gas law holds for pressures until a few atm (1 atm = 1013.25 mbar = 101.325 kPa).

$$pV = nRT \tag{1}$$

Mean free path

The (gas) mean free path "is defined as the average distance traveled by a molecule between successive collisions."(Hinds, 1999, 21)

Considering molecule a, after having collided with molecule b, molecule a travels the mean free path until it collides with molecule c. The (gas) mean free path decreases with increasing density of the gas n, and even stronger with an increasing diameter of the molecule D_m, see equation (2). Not as intuitively is the fact that λ is not directly dependent on the temperature T.

$$\lambda = \frac{1}{\sqrt{2} n \pi D_m^2} \tag{2}$$

The influence of temperature and pressure on the mean free path is 'hidden' in the gas density n, as the transformation of the ideal gas law (1) in equation (3) shows.

$$n = \frac{pV}{RT} \tag{3}$$

Therefore a higher pressure leads to a higher gas density and consequently to a shorter mean free path, the opposite being true for an increase in temperature.

At standard conditions ($p = 1$ atm $= 101.325$ kPa; $T = 293$ K $= 20$ °C), the mean free path of air is $\lambda = 0.066$ μm.

The Knudsen Number (see equation (4)) is a dimensionless quantity, which relates the mean free path λ and the particle diameter D_p. It is directly proportional to the mean free path of a gas λ and inversely proportional to the particle diameter

D_p (Baron and Willeke, 2001; Kulkarni et al., 2011; Hinds, 1999).

$$Kn = \frac{2\lambda}{D_p} \tag{4}$$

In addition and complementary, "[t]he particle mean free path λ_p is defined as the average distance from any origin that the center of a [spherical] particle travels before it completely changes direction."(Hinds, 1999, 154)
As a result, the particle mean free path λ_p, see equation (5), is the product of the stopping distance of the particle τ and its thermal velocity $\bar{v}$ (see equation (6)).

$$\lambda_p = \tau \bar{v} \tag{5}$$

$$\bar{v} = \left(\frac{8kT}{\pi m}\right)^{1/2} = \left(\frac{48kT}{\pi^2 \rho_p D_p^3}\right)^{1/2} \tag{6}$$

In equation (6), k is the Boltzmann constant, T the absolute temperature, m the mass of the particle and ρ_p the density of the particle.

The Reynolds Number

The Reynolds Number is a dimensionless quantity, which describes gas flows in a pipe or around an object. It is the ratio between the inertial force F_I and the frictional force F_f, hence

$$Re = \frac{F_I}{F_f} \tag{7}$$

The useful notation for fluid mechanics, is given by equation (8)

$$Re = \frac{\rho v d}{\eta} \tag{8}$$

where ρ is the density of the gas, η the viscosity, and v the relative velocity between gas and an object with a diameter d. The viscosity η of a gas in units

$[N \cdot s/m^2]$ increases with increasing temperature and is quasi independent of pressure.

The Reynolds number gives insights on the flow profile, whether it is laminar or turbulent. If $Re < 1$, the frictional forces are the dominant ones acting upon the object, for example the aerosol particle, and the flow is laminar. Increasing values of Re describe more turbulent flows (Hinds, 1999).

At standard conditions ($p = 101.325$ kPa; $T = 293$ K $= 20$ °C) and in SI units, the Reynolds number can be determined from the approximation,

$$Re = 66000 \cdot v \cdot d \tag{9}$$

for v in [m/s] and d in [m], using the values for $\rho = 1.20$ kg/m^3 and $\eta = 1.81 \times 10^{-5}$ Pa $\cdot$ s of air.

Newton's Resistance Law

The velocity at which a particle travels in a gas is determined by two competing forces: on the one hand, an external force like gravitation or an electrical force, and on the other hand, the resisting force exerted by the gas, hindering the particles' motion. The strength of this opposing force depends on the relative velocity between particle and gas (Hinds, 1999).

At high Reynolds numbers (> 1000) Newton's resistance law, given in equation (10), is applicable to particle motion.

$$F_D = K \rho_g \frac{\pi}{4} d^2 v^2 \tag{10}$$

The gas resistance force or drag force consists of K, which is a constant of proportionality, ρ_g the density of the gas, d the diameter of the object/particle

and v its velocity. As K was assumed to be independent of v, a more general form of equation (10) including C_D is stated in equation (11).

$$F_D = C_D \frac{\pi}{8} \rho_g d^2 v^2 \tag{11}$$

This expression in equation (11) for the drag force is valid for subsonic particle motion. At high Reynolds numbers (> 1000) $C_D \approx$ const., whereas at smaller Re (< 1000) it becomes a variable (Hinds, 1999).

Stoke's law

Stoke's law, given in equation (12), can be interpreted as a special case of Newton's resistance law (10) & (11), as it describes particle motion at low Reynolds Numbers. This regime is particularly important in aerosol sciences, as particle sizes are small and velocities tend to be low. From equation (7) follows that within this regime inertial forces become negligible compared to the effects of the viscous force exerted on the particle by the gas. It is a solution of the practically unsolvable Navier-Stokes nonlinear partial differential equations, which describe the motion of fluids. His solution was achieved by reducing the partial differential equations to solvable linear equations. For this purpose the following assumptions were made: 1) inertial force can be neglected, 2) incompressibility of the fluid, 3) absence of obstacles, like walls or other particles, 4) the particle has the form of a rigid sphere and 5) the fluid has zero velocity at the surface of the particle (Hinds, 1999).

$$F_D = 3\pi\eta v D_p \tag{12}$$

The resisting force F_D, opposing the particles' motion, given by Stoke's law in equation (12), is directly proportional to the viscosity η of the gas, the velocity v of the particle and its diameter D_p. Using this relationship between F_D and the particle velocity v, it is possible to formulate a particle's mechanical mobility B

(in distinction of the subsequently discussed electrical mobility Z)

$$B = \frac{v}{F_D} = \frac{1}{3\pi\eta D_p} \text{ for } D_p > 1\,\mu m \tag{13}$$

in [m/Ns].

The area where equation (12) holds, is called the Stokes region.
However, Stoke's law underestimates the settling velocity for very small particles ($< 1\,\mu$m), as the assumption of zero velocity at the surface of the particle does not hold. To take this into account, Cunningham introduced a correctional term, the Cunningham correction factor, given by equation (14) (Hinds, 1999).

$$C_c = 1 + \frac{2.52\lambda}{D_p} \tag{14}$$

with λ the mean free path, introduced in equation (2) and D_p the particle diameter.

Stoke's law (12) combined with the Cunningham correction factor (14) leads to equation (15)

$$F_D = \frac{3\pi\eta v D_p}{C_c} \tag{15}$$

But also this extension is limited, as it is only valid for particles with a diameter between $1\,\mu$m and $0.1\,\mu$m. If one considers particles smaller than $0.1\,\mu$m, which is the case in this thesis, the empirically determined slip correction factor is given by equation (16) (Hinds, 1999).

$$C_c = 1 + \frac{\lambda}{D_p}[2.34 + 1.05\exp(-0.39\frac{D_p}{\lambda})] \tag{16}$$

For decreasing pressure, the slip correction becomes larger, due to its direct relation to the mean free path, which also increases with decreasing pressure. Slightly

differing empirical values may be used by different authors.

Brownian Motion and Diffusion

"Excluding convection, thermal diffusion is the primary transport and deposition mechanism for particles less than 0.1 μm in diameter."(Hinds, 1999, 150)
Seinfeld and Pandis (2006) elaborate on the relationship between Brownian motion and diffusion by stating that "[t]he movement of particles due to Brownian motion can also be viewed as a macroscopic diffusion process."(Seinfeld and Pandis, 2006, 415)
A particle suspended in a gas, for example air, has a velocity $v \neq 0$, because constant collisions with ambient air molecules cause random, small displacement effects. Diffusion is always associated with a concentration gradient that leads to a net transfer of particles towards regions of low concentration.

In 1905 Einstein showed that i.a. an aerosol particle and a very large gas molecule have the same observable Brownian motion, and that the aerosol particle experiencing Brownian motion and the molecules of the gas it is suspended in have the same kinetic energy $E_{kin} = \frac{3}{2}kT$ (Hinds, 1999).

Fick's first law of diffusion 17

$$J = -D\frac{dn}{dx} \tag{17}$$

establishes the relation between the flux of aerosol particles J, the diffusion coefficient D and the concentration gradient $\frac{dn}{dx}$. Fick's first law of diffusion in the form of equation (17) is only valid if no external forces are present.

The diffusion force F_{diff} can be equated to Stokes drag force (15), which precisely describes the force exerted on the particle by the gas opposing its motion.

The diffusion coefficient is given by equation (18)

$$D = kTB = \frac{kTC_c}{3\pi\eta D_p} \tag{18}$$

The relationship $D = kTB$ is known as the Einstein relation, with k the Boltzmann constant, T the absolute Temperature and B the mechanical mobility, introduced in equation (13). It includes the slip correction C_c and is therefore applicable for $D_p < 1\mu$m, which is necessary due to the importance of diffusivity for small particles (Seinfeld and Pandis, 2006; Hinds, 1999). From equation (18) follows that diffusivity increases with decreasing particle diameter.

Deposition by Diffusion

For this work, diffusion and deposition effects are of particular interest, because the aerosol passes through several instruments. Furthermore ultrafine particles were generated and investigated, which leads to high diffusion coefficients, as the coefficient is inversely dependent on the particle diameter D_p.

If an aerosol particle hits the surface of an 'obstacle' it adheres to it. A concentration gradient near the surface causes a steady diffusion of particles towards it. Deposition of aerosol particles has the effect of decreasing the particle concentration, which in this work is not desired.

Deposition on a curved surface, in this case a tube with a circular cross section and laminar flow condition is described by the deposition parameter μ, a dimensionless quantity which is given in equation (19).

$$\mu = \frac{4DL}{\pi D_t^2 \bar{U}} = \frac{DL}{Q} \tag{19}$$

Hence, μ is dependent on 1) the length of the tube L, 2) the diffusion coefficient D, 3) the diameter of the tube D_t and 4) the average flow velocity through the tube $\bar{U}$. As $Q = \frac{1}{A\bar{U}}$, where A is the area of the tubes' cross section, $\frac{1}{Q}$ describes the volume flow per unit time, thus the flow rate. Since $\mu \propto D \propto \frac{1}{D_p}$, it follows

that the deposition parameter increases for decreasing particle sizes (Hinds, 1999).

4.2 Basic physical properties

A charge q in an electrostatic field E will experience the force F_E, which is given in equation (20).

$$F_E = qE = neE \tag{20}$$

The charge q can also be written in the form ne with e being the elementary charge (in SI units e $= 1,602 \times 10^{-19}$C) and n the integer number of charges. Therefore the force which acts on a charged particle is determined by the strength of the electrostatic field E and the number of charges n (Hinds, 1999).

Particle Motion in an electric field

By equating 20 and 15 and solving it for the velocity v, the terminal velocity of a charged particle in an electrostatic field can be determined, see equation (21).

$$v_{TE} = \frac{neEC_c}{3\pi\eta D_p} \tag{21}$$

Equation (21) can be further simplified by including the mechanical mobility B, which was introduced in equation (13). The terminal electrostatic velocity may then be expressed as the product of the integer number of charges, the elementary charge, the electrostatic field and the mechanical mobility.

$$v_{TE} = neEB \tag{22}$$

Compared to the mechanical mobility B, the electrical mobility Z describes the way a charged particle travels in an electric field, the relation between the terminal electrostatic velocity v_{TE} of a particle and the electrostatic field E is given by equation (23)

$$Z = \frac{v_{TE}}{E} = \frac{neC_c(D_p)}{3\pi\eta D_p} \text{ for } Re < 1 \tag{23}$$

in units [m^2/Vs] and is therefore a measurement unit for the velocity of the particle per unit of electrical field strength. In other words, when a charged particle enters an electric field, its velocity is determined by the electrostatic force of the field and the aerodynamic drag which opposes the motion (Hinds, 1999; Baron and Willeke, 2001; Kulkarni et al., 2011). The electrical mobility is both dependent on particle size and charging state, meaning the number of charges the particle carries.

Equation (24) shows the relationship between mechanical and electrical mobility which is

$$Z = qB = neB \tag{24}$$

(Hinds, 1999; Seinfeld and Pandis, 2006).

Particle shape and diameter

For the purpose of simplicity, spherical particles are usually assumed in theory, which is not necessarily the case in reality. It is crucial at this point to discuss the notion of particle shape and diameter within this context.

There are basically four main concepts of diameter in aerosol physics.

1. The volume equivalent diameter d_e

   "The volume equivalent diameter [...] is the diameter of a sphere having the same volume as the given nonspherical particle"(Seinfeld and Pandis, 2006, 426), see equation (25).

$$d_e = \frac{6}{\pi} V_p^{1/3} \tag{25}$$

2. The aerodynamic equivalent diameter d_a

   The aerodynamic equivalent diameter d_a is the diameter of a sphere with a density of $\rho_p = 1\ g/cm^3 = 1000\ kg/m^3$ and the same terminal velocity v_t as the actual particle of unknown shape.

$$d_a = \left(\frac{18 v_t \eta}{\rho_p g C_c(d_a)} \right)^{1/2} \tag{26}$$

3. The Stokes equivalent diameter d_s

   The Stokes diameter d_s describes a sphere with the same terminal velocity v_t and density ρ_p as the actual particle of unknown shape.

$$d_s = \left(\frac{18 v_t \eta}{\rho_p C_c(d_s)} \right)^{1/2} \tag{27}$$

4. The electrical mobility equivalent diameter d_Z

   The electrical mobility equivalent diameter d_Z is the diameter of a sphere with unit density and the same electrical mobility Z as the actual particle of unknown shape.

$$d_Z = \frac{ne}{3\pi\eta} \frac{C_c(d_Z)}{Z} \tag{28}$$

For spherical particles $d_e = d_s = d_p$ is given, meaning that the actual physical diameter of the particle is the same as the volume equivalent and Stokes equivalent diameter, however the aerodynamic equivalent diameter d_a may differ as it is defined for a sphere with unit density, which is also true for the electrical mobility equivalent diameter (Seinfeld and Pandis, 2006; Hinds, 1999).

Nonspherical particles show a different behavior than spheres, which is accounted for by the dynamic shape factor χ, given in equation (29). It can be interpreted

as a correction to Stokes law (15), if the particles are not spheres. It is the ratio between the drag force of the nonspherical, actual particle and the drag force of a particle with an equivalent volume diameter d_e (Hinds, 1999; Seinfeld and Pandis, 2006).

$$\chi = \frac{F_D}{3\pi\eta v d_e} = \frac{F_D}{F_D(d_e)} \tag{29}$$

4.3 Aerosol Charging/Neutralization

There are different mechanisms for aerosol charging, among other processes static electrification, diffusion charging and field charging (Hinds, 1999). The charging/neutralization devices used for the experimental work for this thesis, introduced in chapter 5, are all based on diffusion charging. Even though there is one significant distinction, chargers based on radioactive materials and soft X-rays are bipolar chargers, and produce positive and negative ions. The probably simplest and most straight-forward way to realize a unipolar charger, i.e. produce ions of only one sign, is by corona discharge.

The process of diffusion charging is governed by thermal diffusion as discussed towards the end of section 4.1 (Hinds, 1999; Baron and Willeke, 2001).
If aerosol particles are mixed with unipolar ions, collisions between particles and ions occur due to the random Brownian motion of both, even if no external field is present. The charge of the ion then transfers to the particle, and as the particles accumulate more charges, a field establishes. The field prevents the accumulation of additional charges and therefore reduces the charge rate. The number of ions with high enough velocities to overcome the repulsive force decreases, even though it never reaches zero because ions have a Boltzmann distribution of velocities, which does not have an upper limit.

Equation (30) describes the time dependent acquisition of charges by particles due to diffusion charging. $\bar{v_i}$ denotes the mean thermal speed, N_i the concentration of the ions and $K_E = \frac{1}{4\pi\epsilon_0}$, with ϵ_0 being the vacuum permittivity (Hinds, 1999).

$$n(t) = \frac{D_p kT}{2K_E e^2} ln[1 + \frac{\pi K_E D_p \bar{v_i} e^2 N_i t}{2kT}] \tag{30}$$

Equation (30) is valid for particles with a diameter $D_p = 70$ nm - 1.5 μm and a $N_i t$ product $> 10^6$ s/cm^3 up to a factor 2. For $D_p = 50$ nm - 40 μm, a $N_i t$ product $> 10^7$ s/cm^3 is necessary for an accuracy by a factor 2. The $N_i t$ product specifies the residence time of the aerosol particles/clusters and the required amount of ions to bring the aerosol in a well-defined charge state. For particles with $D_p \leq 200$ nm, diffusion charging is the main charging mechanism (Hinds, 1999).

Diffusion charging within a bipolar ion environment is governed by two (competing) processes. On the one hand, previously uncharged particles/clusters get charged and/or acquire additional charges. On the other hand, charged particles/clusters get neutralized or reduced in their charge state by the attraction and attachment of ions of opposite sign. Usually, one may assume almost equal amounts of negative and positive ions, even though their properties differ. After a certain time, the so-called Boltzmann equilibrium charge distribution establishes. "The Boltzmann equilibrium charge distribution represents the charge distribution of an aerosol in charge equilibrium with bipolar ions. "(Hinds, 1999, 335)

The Boltzmann charge distribution based on the assumption of equal amounts of positive and negative ions is given in equation (31), where f_n denotes the fraction of monodisperse particles with n units of charge (either positive or negative). It includes the statistical probability for uncharged and for multiply charged particles.

$$f_n = \frac{exp(K_E n^2 e^2 / D_p kT)}{\sum_{n=-\infty}^{\infty} exp(K_E n^2 e^2 / D_p kT)} \tag{31}$$

This approximation is only valid for particles of $\gtrsim 0.05\,\mu$m as it underestimates the charged fraction of particles at lower sizes (Hinds, 1999; Hoppel and Frick, 1986).

Reischl et al. (1996) state $0.03\,\mu$m as the threshold where the Boltzmann equilibrium charge distribution significantly underestimates this fraction. Equation (32) is an empirical approximation that states the average amount of charges a particle with a diameter D_p [μm] has. For particles $D_p > 0.2\,\mu m$, the approximation is sufficiently accurate.

$$\bar{n} \approx 2.37\sqrt{D_p} \tag{32}$$

Equation (33) is a function of time and ion concentration, and gives the rate for reaching the Boltzmann equilibrium charge distribution. The $N_i t$ product specifies at which bipolar ion concentration N_i and after what time t the aerosol reaches the Boltzmann equilibrium (Hinds, 1999).

$$\frac{n(t)}{n_0} = exp(-4\pi K_E e Z_i N_i t) \tag{33}$$

It is important to emphasize on the fact that the rate does not depend on the particle size nor on the initial charge state. Therefore it is possible to determine the charge state of an aerosol after leaving a charging/neutralizing device without the knowledge of its initial charge state.

Hoppel and Frick (1986) state two major shortcomings of the Boltzmann distribution, namely "i) it fails at small particle sizes and ii) it does not yield absolute values of the ion-aerosol attachment coefficients."(Hoppel and Frick, 1986, 2)

To account for smaller particles Fuchs (1963) introduced a new charge theory,

which unlike the Boltzmann distribution is applicable to steady-state rather than to equilibrium processes.

From a theoretical point of view the charge distribution of a bipolar ion environment has to be treated as a stationary state process and not an equilibrium one, and the Boltzmann equation only describes the latter.

If an aerosol mixes with a high number of ions, a stationary state establishes after a given period of time. It is said to be stationary, as the net charge over all particles does not change, even though charge transfer still happens by collisions with ions (Fuchs, 1963). The method of the limiting sphere was used by Fuchs (1963) to calculate the combination coefficients for gaseous ions and aerosol particles. It allows to apply the theory not only to the continuum ($Kn_{ion} \rightarrow 0$), but also the transition ($0.1 < Kn_{ion} < 10$) and the free molecule regime ($Kn_{ion} \rightarrow \infty$).

The limiting sphere is a concentric sphere surrounding the particle, its radius is approximately $r_{lim} = r_p + \lambda_{ion}$. The continuum regime applies to the outside of the limiting sphere, where ion movement is explained by diffusion-mobility theory. The movement and trajectories of ions entering the limiting sphere are described by kinetic gas theory and Hamiltonian dynamics. Ions moving inside the limiting sphere are assumed to travel like in a vacuum, meaning that collisions with other ions are excluded.

The necessary ion properties to calculate the charging probability are: electrical mobility $Z^{\pm}_{ion}$, ion mass $m^{\pm}_{ion}$, the diffusion coefficient $D^{\pm}_{ion}$, the mean thermal velocity of the ion $\bar{v}^{\pm}_{ion}$ and the mean free path $\lambda^{\pm}_{ion}$. Although in Fuchs theory all ion properties can be derived from the two parameters: electrical mobility and mass (Fuchs, 1963; Reischl et al., 1996). Despite the lack of one unique theoretical well-established relationship between ion mobility and mass, there are conversion procedures using empirical data to estimate ion masses from electrical mobilities, e.g. the mass mobility relationship established by Kilpatrick (1971) and more cur-

rent findings by Ku and Férnandez de la Mora (2009) and Steiner et al. (2014). To obtain accurate results for the charging probabilities, it is necessary to include differences between negative and positive ion properties. Otherwise the charging probabilities for both polarities are symmetrical, which is experimentally proven to be incorrect (Reischl et al., 1996). Averages for ion mobilities from various experimental data provided by Reischl et al. (1996) are

$$Z^+ = 1.33 cm^2/Vs \tag{34}$$

for positive ions and for negative ions

$$Z^- = 1.84 cm^2/Vs \tag{35}$$

and estimated masses from mass-mobility correlations

$$m^+ \simeq 200\, amu \tag{36}$$

and

$$m^- \simeq 100\, amu \tag{37}$$

Reischl et al. (1996) state that the calculated charging probabilities using Fuchs theory are in best agreement with their experimentally obtained data when using:
$Z^+ = 1.15$ cm^2/Vs
$Z^- = 1.43$ cm^2/Vs
$m^+ = 290$ amu
$m^- = 140$ amu

A more recent study by Kallinger et al. (2012) investigates ion mobilities for four different aerosol neutralizers and find ion el. mobilities

- for the ^{241}Am source: $\bar{Z^+} = 1.5$ cm^2/Vs and $\bar{Z^-} = 2.09$ cm^2/Vs

- for X-ray: $\bar{Z^+} = 1.55$ cm^2/Vs and $\bar{Z^-} = 1.69$ cm^2/Vs
- for an AC-corona discharge device : $\bar{Z^+} = 1.57$ cm^2/Vs and $\bar{Z^-} = 1.85$ cm^2/Vs
- for a TSI advanced aerosol neutralizer (soft X-ray): $\bar{Z^+} = 1.6$ cm^2/Vs and $\bar{Z^-} = 1.68$ cm^2/Vs

as mean values.

Tigges et al. (2015a) provide a selection of published values for ion mobilities dating from 1971 to 2012.
The last part of section 5.2 discusses charger ion properties and their influence on electrical mobility measurements in more detail.

In these experiments a stationary state was not necessarily achieved, because the designated flow rates for the neutralizers were exceeded many times over and therefore the residence time t of the aerosol particles/clusters was brief. Furthermore, this was not desirable in this case, since it would have been too effective as the charging probabilities for the i-mers are extremely low. To reach a stationary state means that all the clusters get neutralized.

5 Methods and Instrumentation

Section 5 introduces the instrumentation for the aerosol measurements. The structure of the chapter follows the experimental setup, starting with the particle generation and the measurement substances, continuing with the neutralization techniques, the classification, and finally the detection.

5.1 Particle/Cluster Generation

Electrospray (ES)

The electrospray (ES) allows the generation of well-defined particles and molecular clusters in the sub 10 nm size range.

The liquid solution that is meant to be atomized is raised to a high voltage potential. The dissolved ions migrate towards the counter electrode. The liquid forms a cone-like shape, called the Taylor cone (Taylor, 1964), due to the competing forces of the liquid's surface tension and the electrical forces. If the electrical field is strong enough to overcome the surface tension of the liquid, a jet of highly charged droplets is released. The jet mixes with the carrier gas, subsequently the solvent evaporates on the way towards the counter electrode and smaller droplets remain, which is indicated in figure 2. The high number of charges in the narrowly confined volume leads to droplet fission, the Coulomb explosion, at the Rayleigh limit, see equation (38) with n_L being the limiting charge.

$$n_L = \left(\frac{8\pi^2 \epsilon_0 \sigma D_p^3}{e^2} \right)^{1/2} \tag{38}$$

σ refers to the surface tension of the droplet, D_p is the particle diameter, ϵ_0 the permittivity of a vacuum and e the elementary charge. The Rayleigh limit is reached when the repulsive forces of the charges within the droplet exceed the surface tension of the liquid droplet (Hinds, 1999; Gamero-Castaño and Fernández

de la Mora, 2000; Rosell-Llompart and Fernández de la Mora, 1994).

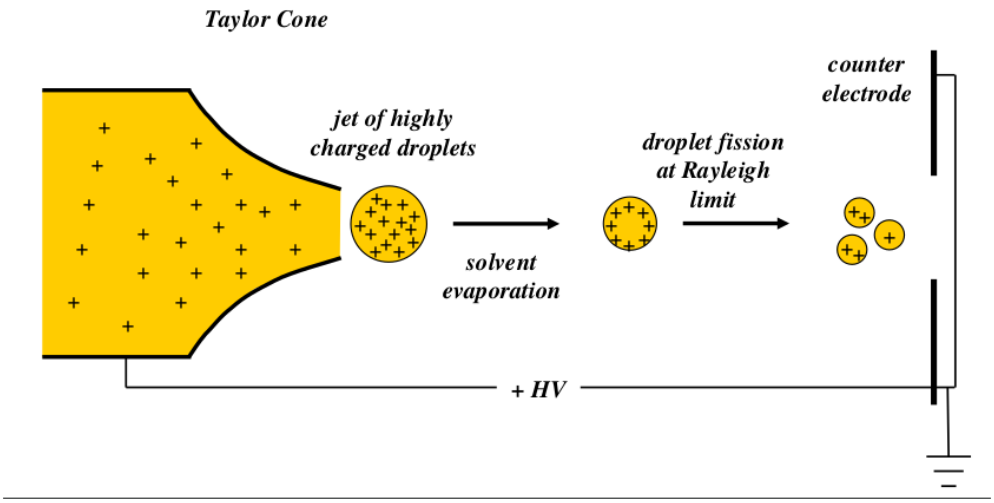

Figure 2: Electrospray working principle: if the electrostatic field is high enough, a jet of highly charged droplets is released. On the way towards the counter electrode the solvent evaporates and the charges remain in a narrowly confined volume resulting in a Coulomb explosion at the Rayleigh limit. The figure was taken from Steiner (2011, 66).

A high number of singly charged particles/clusters but also a significant amount of multiply charged ones remain, which can be classified directly by e.g. a differential mobility analyzer (DMA) or may pass through an aerosol neutralizer first. For the following experiments the electrospray shown in figure 3 was used. It is similar to the design by Rosell-Llompart and Fernández de la Mora (1994), but with a high resolution microscope camera. For a more detailed discussion of the optical system, see the diploma thesis of Wimmer (2008).

The ES consists of an electrospray chamber, a capillary, a high voltage supply, a vial containing the to be atomized liquid solution, a pressure supply, and a camera to monitor the tip of the capillary to monitor potential contaminations or blockages and whether or not the electrospray is working in a stable manner.

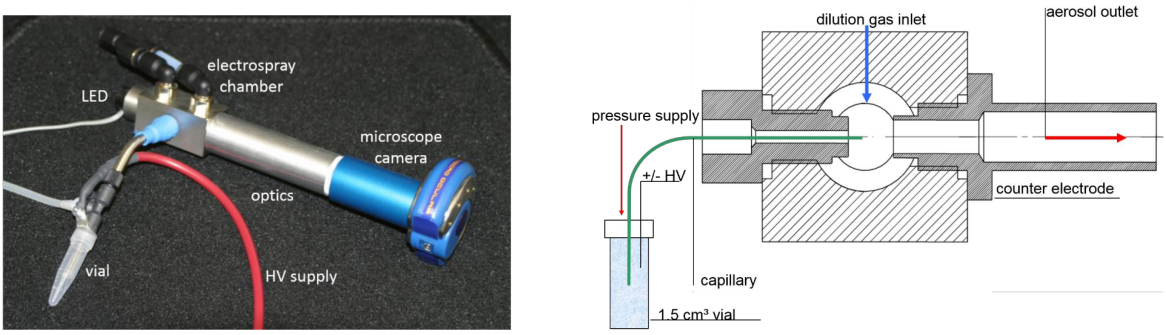

Figure 3: The figure on the left hand side shows a photograph of the ES used in the experiments. The figure on the right hand side shows the scheme of the ES (Steiner, 2011, 67f).

On the right of figure 3 a sketch of the ES is shown.

The green line refers to the capillary, made of fused silica with an inner diameter of 40 μm, and an outer diameter of 360 μm purchased from New Objective. The electrospray chamber is made of stainless steel.

The liquid solution follows the pressure gradient through the capillary, which pushes it towards the tip. As shown in figure 3 the analyte solution in the vial is raised to a voltage of 1 to 3 kV by a platinum wire immersed into the solution. The dissolved ions migrate towards the counter electrode, and the Taylor cone is formed at the tip of the capillary. The tip is sharpened to conical shape to facilitate the formation of the Taylor cone.

Tetra-alkyl ammonium halide salts (TAAHS) and Ionic liquid

The solutions in these experiments were mainly tetra-alkyl ammonium halide salts dissolved in acetonitrile. High purity alcohols like methanol and ethanol can be also used as solvents. These rather large organic salts serve as mobility standards, and can be used to calibrate and evaluate instruments like DMAs (Ude and Fernández de la Mora, 2005).

For the subsequently discussed experiments in section 6 three tetra-alkyl ammonium halide salts, tetraheptyl ammonium bromide (THABr), tetrabutyl ammonium iodide (TBAI), and tetrapropyl ammonium iodide (TPrAI) as well as one so-called ionic liquid, Methyltrioctylammonium bis(trifluoromethylsulfonyl)imide (MTOA - BF3I) were used, purchased by Sigma Aldrich and io-lite tech respectively.

These substances produce a spectrum of consecutive sharp peaks in the form of $A^+(AB)_m$ and $B^-(AB)_n$ in the mobility spectrum, where each peak can be assigned to a specific cluster species, which furthermore allows the determination of the electrical mobility equivalent diameter of it. The first sharp peak, at the smallest inverse electrical mobility ($1/Z$) is the monomer of the salt, hence the bare cation (A^+) or anion (B^-), depending on the polarity applied to the ES. The second peak is the dimer, which is the cation with one neutral tetra-alkyl ammonium molecule ($(A^+)(AB)_1$), followed by the trimer ($(A^+)(AB)_2$) and so on (Ude and Fernández de la Mora, 2005).

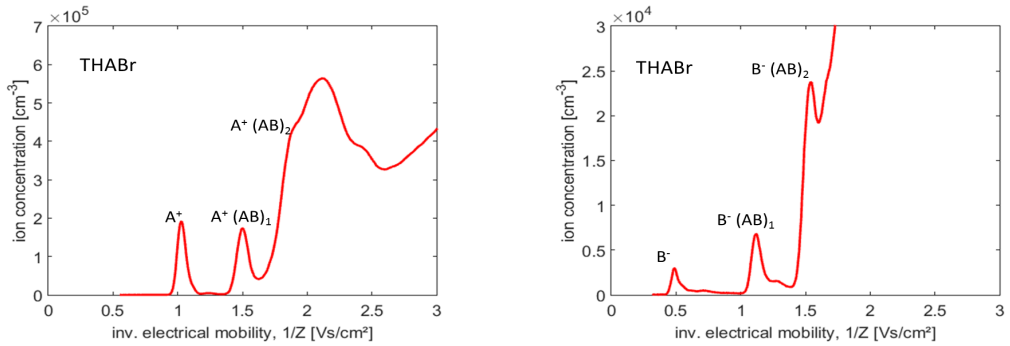

(a) Positive spray: THABr electrical mobility spectrum

(b) Negative spray: THABr electrical mobility spectrum

Figure 4: Example of a positive electrical mobility spectrum of THABr (left) and a negative one (right). Subsequent to the generation by the electrospray, the clusters were directly forwarded to the DMA, without passing a neutralizer first. The anion B^- on the right is the bromine atom itself.

Table 1 to 10 illustrate the properties of the substances, to understand what the peaks in the electrical mobility spectra effectively depict. The values for inverse mobility [Vs/cm^2] and electrical mobility equivalent diameter [nm] are presented in the result section 7 of this thesis in tables 9 and 10.

1. **THABr** Tetraheptyl ammonium bromide $N[C_7H_{15}]_4Br$

ion	config.	formula	m [amu]
THABr	$(A^+)(AB)_0$	$C_{28}H_{60}N^+$	410.47
	$(A^+)(AB)_1$	$C_{56}H_{120}N_2Br^+$	901.64
	$(A^+)(AB)_2$	$C_{84}H_{180}N_3Br_2{}^+$	1392.34
	$(A^+)(AB)_3$	$C_{112}H_{240}N_4Br_3{}^+$	1883.03
	$(A^+)(AB)_4$	$C_{140}H_{300}N_5Br_4{}^+$	2373.73

Table 1: Positive spray of THABr: configuration, according formula and mass

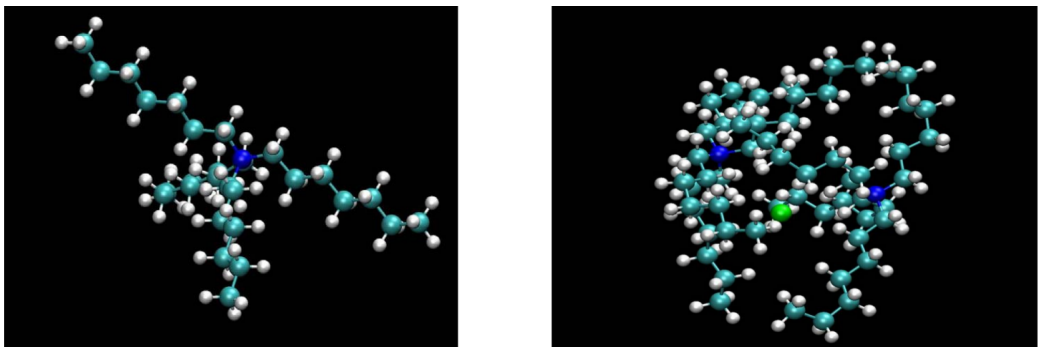

(a) Monomer of THABr (positive)

(b) Dimer of THABr (positive)

Figure 5: The molecular structure of the monomer and dimer of THABr. Simulated with the programme "ChemBioOffice Ultra 2010 12.0" from "CambridgeSoft®" taken from the dissertation of Steiner (2011, 73).

Figure 5 shows the molecular structure of the monomer ($(A^+)(AB)_0$) and dimer ($(A^+)(AB)_1$) of THABr. The nitrogen atoms are the dark blue spheres, which are surrounded by the carbon atoms in cyan and the hydrogen atoms in white. For the dimer, on the right, the bromide is depicted in green. The structures of TBAI and TPrAI are similar, only differing in the number of carbon and hydrogen atoms and the halide in green would be iodide instead of bromide.

ion	config.	formula	m [amu]
THABr	$(B^-)(AB)_0$	Br^-	78.92
	$(B^-)(AB)_1$	$C_{28}H_{60}NBr_2{}^-$	568.31
	$(B^-)(AB)_2$	$C_{56}H_{120}N_2Br_3{}^-$	1057.70
	$(B^-)(AB)_3$	$C_{84}H_{180}N_3Br_4{}^-$	1547.09
	$(B^-)(AB)_4$	$C_{112}H_{240}N_4Br_5{}^-$	2036.48

Table 2: Negative spray of THABr: configuration, according formula and mass

2. **TBAI** Tetrabutyl ammonium iodide $N[C_4H_9]_4I$

ion	config.	formula	m [amu]
TBAI	$(A^+)(AB)_0$	$C_{16}H_{36}N^+$	242.28
	$(A^+)(AB)_1$	$C_{32}H_{72}N_2I^+$	611.47
	$(A^+)(AB)_2$	$C_{48}H_{108}N_3I_2{}^+$	980.66
	$(A^+)(AB)_3$	$C_{64}H_{144}N_4I_3{}^+$	1349.85

Table 3: Positive spray of TBAI: configuration, according formula and mass

ion	config.	formula	m [amu]
TBAI	$(B^-)(AB)_0$	I^-	126.90
	$(B^-)(AB)_1$	$C_{16}H_{36}NI_2{}^-$	496.09
	$(B^-)(AB)_2$	$C_{32}H_{72}N_2I_3{}^-$	865.28
	$(B^-)(AB)_3$	$C_{48}H_{108}N_3I_4{}^-$	1234.47

Table 4: Negative spray of TBAI: configuration, according formula and mass

3. **TPrAI** Tetrapropyl ammonium iodide $N[C_3H_7]_4I$

ion	config.	formula	m [amu]
TPrAI	$(A^+)(AB)_0$	$C_{12}H_{28}N^+$	186.22
	$(A^+)(AB)_1$	$C_{24}H_{56}N_2I^+$	499.35
	$(A^+)(AB)_2$	$C_{36}H_{84}N_3I_2{}^+$	812.48
	$(A^+)(AB)_3$	$C_{48}H_{112}N_4I_3{}^+$	1125.60

Table 5: Positive spray of TPrAI: configuration, according formula and mass

ion	config.	formula	m [amu]
TPrAI	$(B^-)(AB)_0$	I^-	126.90
	$(B^-)(AB)_1$	$C_{12}H_{28}NI_2{}^-$	440.03
	$(B^-)(AB)_2$	$C_{24}H_{56}N_2I_3{}^-$	753.16
	$(B^-)(AB)_3$	$C_{36}H_{84}N_3I_4{}^-$	1066.28

Table 6: Negative spray of TPrAI: configuration, according formula and mass

4. **MTOA - BF3I** Methyltrioctylammonium bis(trifluoromethylsulfonyl)imide $C_{27}H_{54}F_6N_2O_4S_2$

MTOA - BF3I is an ionic liquid with a molar mass of 648.55 g/mol, a density of 1.11 g/cm^3, and a melting point at -50°C (Steiner et al., 2017). Both positive and negative molecular clusters were generated by electrospraying MTOA - BF3I in acetonitrile as a solvent. The result is a pattern of consecutive sharp peaks similar to the spectra of the tetra-alkyl ammonium halide salts. Table 9 and 10 list configuration, formula and mass of the positively and negatively charged clusters of MTOA - BF3I.

ion	config.	formula	m [amu]
MTOA	$(A^+)(AB)_0$	$C_{25}H_{54}N^+$	368.43
	$(A^+)(AB)_1$	$C_{52}H_{108}N_3O_4F_6S_2$	1016.77
	$(A^+)(AB)_2$	$C_{79}H_{162}N_5O_8F_{12}S_4$	1665.11
	$(A^+)(AB)_3$	$C_{106}H_{216}N_7O_{12}F_{18}S_6$	2313.45
	$(A^+)(AB)_4$	$C_{133}H_{217}N_9O_{16}F_{24}S_8$	2961.80

Table 7: Positive spray of MTOA - BF3I : configuration, according formula and mass

ion	config.	formula	m [amu]
MTOA	$(B^-)(AB)_0$	$C_2NO_4F_6S_2$	279.92
	$(B^-)(AB)_1$	$C_{29}H_{54}N_3O_8F_12S_4$	928.26
	$(B^-)(AB)_2$	$C_{56}H_{108}N_5O_12F_18S_6$	1576.60
	$(B^-)(AB)_3$	$C_{83}H_{162}N_7O_16F_24S_8$	2224.95
	$(B^-)(AB)_4$	$C_{110}H_{216}N_9O_{20}F_{30}S_{10}$	2873.29

Table 8: Negative spray of MTOA - BF3I : configuration, according formula and mass

For the majority of the experiments these substances were diluted in acetonitrile (C_2H_3N). The molar concentration of the dilution was partly varied if necessary. Meaning that lower molar concentrations (compared to the standard 1 mMol/L dilution for the tetra-alkyl ammonium halides and 7 mmol/L for MTOA - BF3I) were applied to increase the signal of monomer and dimer, especially in the negative spraying mode, and when working with the soft X-ray charger, due to an increase in diffusion losses associated with the length of the device.

The major advantage and application possibility of tetra-alkyl ammonium halide salts as mobility standards is for instruments calibration down to sizes below 10 nm as well as the analysis of their performance and resolution (Ude and Fernández

de la Mora, 2005; Steiner et al., 2010; Jiang et al., 2011).
As Ude and Fernández de la Mora (2005) put it, "[ionic size standards] have provided a feedback without which it would have been very difficult to reach current DMA resolving powers at nanometer sizes"(Ude and Fernández de la Mora, 2005, 1225).

5.2 Neutralization of particles/clusters

Bipolar chargers/neutralizers use ionizing radiation e.g. in form of X-rays or from radionuclides.
The carrier gas molecules are ionized, and form primary ions. If an electron is ejected from an ambient gas molecule or a stable atom, a positive ion is formed. If a molecule or stable atom captures a free electron, a negative ion results (Baron and Willeke, 2001; Hinds, 1999). Subsequently larger ion clusters are formed by the combination of the primary ions with the most abundant compounds and water in the carrier gas. The 'secondary' ion clusters then interact with the incoming aerosol resulting in a well-defined charging state of the aerosol (Steiner and Reischl, 2012).
Aerosol charging is necessary in order to establish a well-defined charge distribution without the knowledge of its initial charging state. This is imperative for determining the according size distribution (Hinds, 1999; Hernandez-Sierra et al., 2003; Intra and Tippayawong, 2009).
The three best-known ways of charging/neutralizing aerosol particles/clusters are: soft X-rays, radioactive sources and corona discharge. All based on the process of diffusion charging/neutralization as described in section 4.3, and used for the experiments presented in section 6.
Aerosol charging based on bipolar charging devices like a soft X-ray or a radioactive ionizer is governed by two processes. On the one hand, previously uncharged

particles/clusters acquire a charge, and on the other hand, charged ones are being neutralized or reduced in their charging state by the attraction and attachment of ions of opposite sign.

Since the charging probability is directly proportional to the particle diameter and the charging efficiency of a bipolar ionizer is limited due to the charging - neutralization effect, unipolar ionizers are used to enhance charging probabilities if working with nanoparticles. The most common way to produce ions of one polarity is based on corona discharge (Hinds, 1999; Hernandez-Sierra et al., 2003; Intra and Tippayawong, 2009).

Radioactive Ionizer - ^{241}Am

Ionizing radiation from radionuclides produces bipolar ions by ejecting electrons from ambient molecules or atoms.

An α emitter generates approximately 1 ion pair/35.5 eV (Cooper and Reist, 1973; Baron and Willeke, 2001). "Because of its high mass, an alpha particle produces dense ionization along a straight and relatively short path."(Cooper and Reist, 1973, 20)

α particles are emitted at one specific energy, the exact value is characteristic for the radionuclide.

For the experimental work an ^{241}Am was used as a radioactive ionizer. Other radionuclides like ^{85}Kr, ^{210}Po and ^{63}Ni may be used as well, though the long half-life distinguishes ^{241}Am from the other materials (Tigges et al., 2015b; Steiner and Reischl, 2012, e.g.).

^{241}Am is an alpha emitter with a half life $T_{1/2}$ of 432.2 years. ^{241}Am decays into ^{237}Np by α emission at 5.5 MeV and a small amount of γ radiation (Steiner and Reischl, 2012).

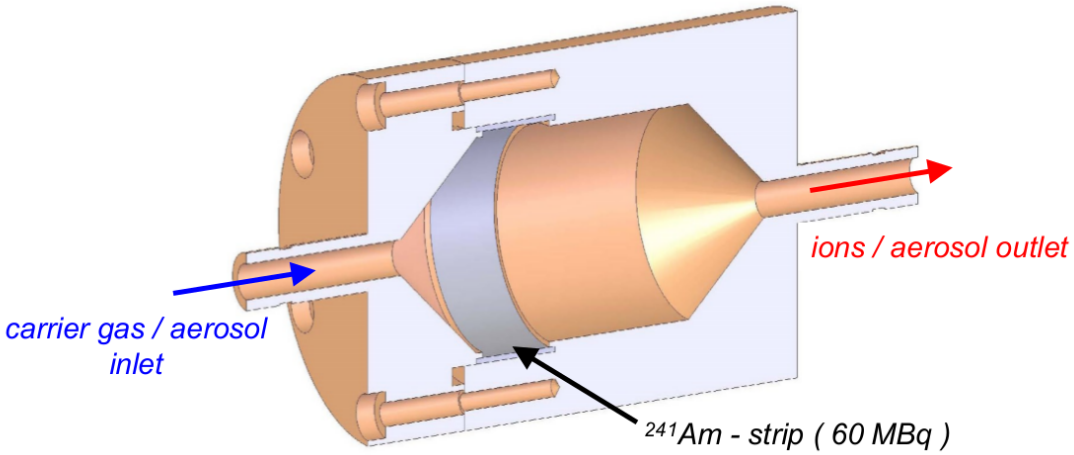

Figure 6: Schematic cross section of the ^{241}Am neutralizer, (Steiner, 2011, 89)

In figure 6, the schematic cross section of the ^{241}Am neutralizer by "tapcon & analysesysteme" is shown, which was used for the first part of the experiments presented in section 6. As outlined in figure 6, the radioactive material, in this case ^{241}Am, is coated onto a strip, and mounted on a silver matrix. The surrounding housing consists of stainless steel. The activity of the radionuclide is 60 MBq = 1.62 mCi.

The residence time t of the aerosol within the charger was extremely short. For the two aerosol inlet flow rates of 16 and 14 L/min, see section 6.1, and a charger volume of about 32 cm^3, $t \approx 0.12$ s and 0.14 s respectively. Therefore the number of ions N_i has to be high in order to have a significant impact.

The main downside of using a radioactive source as an aerosol neutralizer/charger are the very strict legal regulations concerning the handling, and transport. Another drawback, which sometimes can be impractical, is that it is not possible to turn off the device.

Soft X-Ray (SXR)

The soft X-ray charger is a bipolar diffusion charger based on ionizing radiation.

The ambient air molecules are ionized by soft x-rays at energies < 9.5 keV.

On the left hand side of figure 7, a sketch of the basic function of the TSI "Advanced Aerosol Neutralizer Model 3078" soft X-ray neutralizer, and the underlying principle of bipolar diffusion charging is shown. The source, in this case a soft X-ray source at the very top, ionizes the carrier gas molecules, and forms ions. If an electron is ejected from an ambient gas molecule or a stable atom a positive ion is formed. If a molecule or stable atom captures a free electron, a negative ion results. Virtually the same amount of positive and negative ions are produced (Hinds, 1999).

The aerosol enters at the bottom (figure 7), and gets neutralized by interacting with the abundant ambient ions. If the residence time t of the aerosol within the neutralizer is long enough it reaches a steady state charge distribution.

Depicted on the right hand side of figure 7 is the soft X-ray charger which was used for the experiments presented in section 6. The overall length of the TSI "Advanced Aerosol Neutralizer Model 3078" is 39.4 cm, whereby the path to be travelled by the electrospray generated clusters is approximately 22 ± 1 cm. It can easily be switched on and off with an approximate response time of 7 s. According to the manufacturer, it neutralizes excessive charges for concentrations up to 10^7 particles/cm^3, and induces a well defined steady state charge distribution on the aerosol. The specified flow rate range lies between 0.3 - 5.0 L/min. The maximum value of 5.0 L/min was exceeded up to 4 times over for the following experiments introduced in section 6. The efficiency of the device is therefore diminished, as the ideal values of the $N_i t$ product could not have been realized, as t decreases with an increasing flow rate.

The main drawback of the soft X-ray charger, especially when working with very small particles/molecular clusters, is the length of the device. In order to avoid diffusion losses, the path to be traveled by the particles/clusters, should be

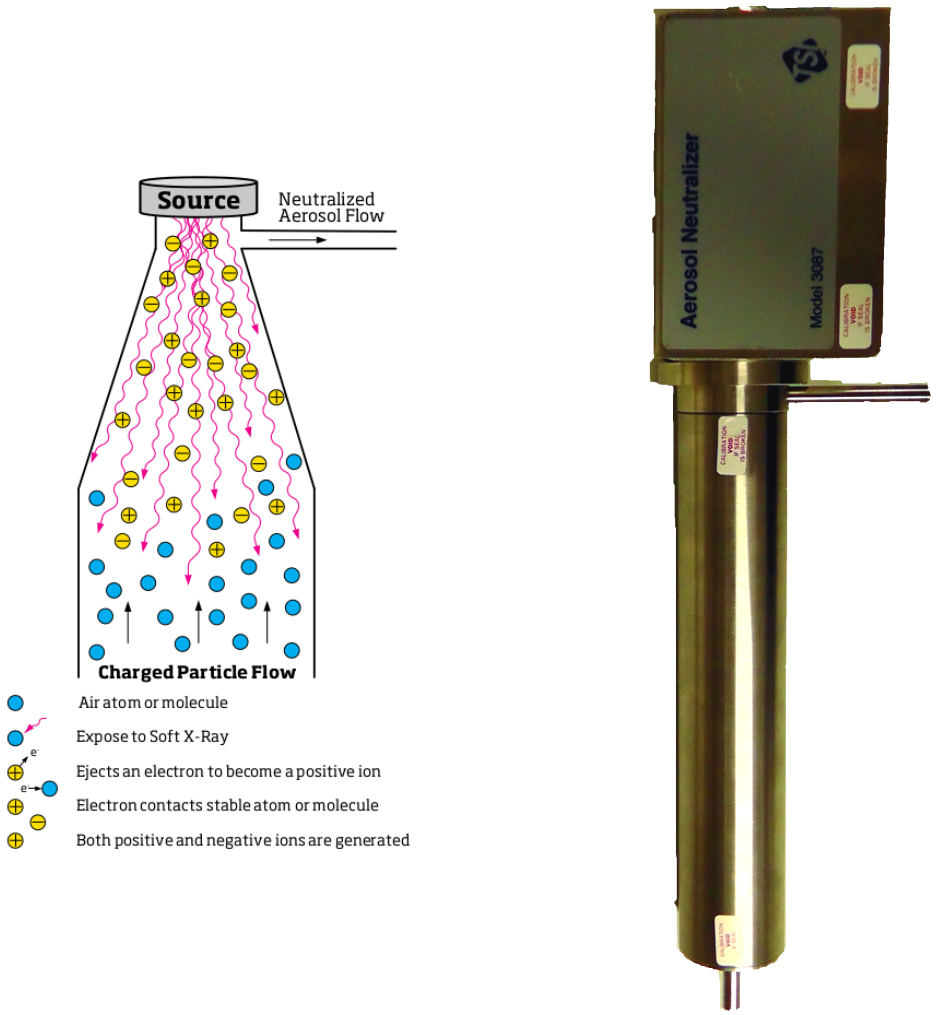

Figure 7: On the left side is a sketch of the operating principle, taken from the TSI manual for the "Advanced Aerosol Neutralizer" Model 3087 (TSI, 2012). The right figure shows the soft X-Ray "Advanced Aerosol Neutralizer" from TSI, Model 3087, which was used for the experiments.

minimal to realize measurable concentrations.

All technical specifications are taken from the instrument manual provided by the manufacturer (TSI, 2012).

Corona ionizer

Corona discharge is a convenient way of continuously producing high number concentrations of unipolar ions. This means that larger particles can acquire more charges over time compared to the case with bipolar ions, as the possibility of a charged particle to attract a charge of the opposite sign due to the attractive forces is high. Also the possibility of smaller particles to get charged increases with the prevention of possible neutralization (Baron and Willeke, 2001).

There are basically two ways to realize a corona discharge. First, between a needle and a plate or second, between a concentric wire and a tube. For both configurations the necessary nonuniform electrostatic field can be established (Hinds, 1999; Intra and Tippayawong, 2009).

The continuous generation of ions must be guaranteed as their lifetimes are brief. For the following experimental work, see section 6, a corona construction with a needle was chosen.

If the potential, at which the needle or wire is being held is high enough the air surrounding the tip (needle), respectively the surface (wire) becomes conductive. The region where this electrical breakdown occurs, is called the corona discharge region. Within this region, free electrons are accelerated, and achieve high enough velocities to knock out electrons from carrier gas molecules. Electrons and positive ions result. If the needle or wire runs on positive high voltage, the positive ions are repelled from it and the free electrons are attracted, whereas the other way around is true for negative high voltage. For the latter case, the electrons decelerate as

the field decreases with increasing distance from the needle/wire, and may attach to carrier gas molecules and therefore create negative ions. The production of a unipolar ion region is hence based on charge separation.
The aerosol particles may either pass directly through the area between needle and plate (respectively wire and tube) or an additional air stream moves the ion cloud to a mixing region, where ions and aerosol particles then interact (Hinds, 1999; Baron and Willeke, 2001).
Unlike in bipolar charging, no steady state is reached in unipolar charging.
For a corona neutralizer the charge distribution is defined by the geometry of the charging device and the operation conditions (Alguacil and Alonso, 2006).

For this line of work a custom-made corona charger was built, shown in figure 9. It consists of two parts, both stainless steel sealed with a viton o-ring.
It is based on a simple design, following the findings of amongst others Hernandez-Sierra et al. (2003), Alonso et al. (2006) or Alguacil and Alonso (2006) that very sophisticated designs do not necessarily yield better results. Figure 8 shows the cross section of the newly built corona charger, with the high voltage connection at the very top, followed by a horizontally aligned gas inlet, a circular peek flow shaper with a small pointlike aperture at the center, where the corona needle is tucked in, and concentrically arranged apertures, which shape the particle free compressed air stream which moves the ion cloud to the mixing area, see figure 9.

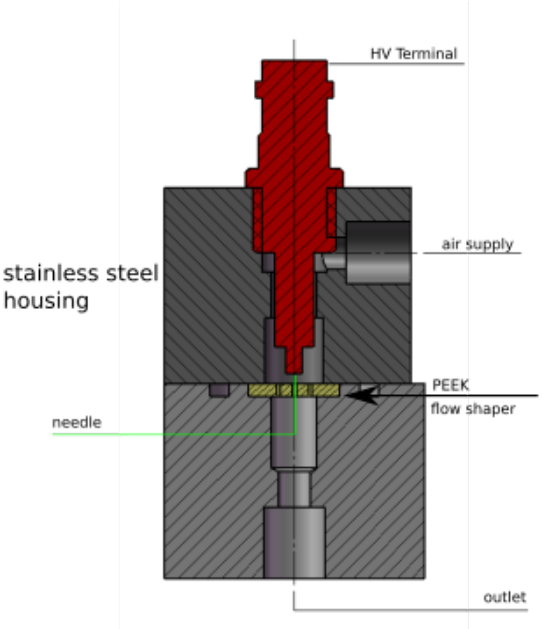

Figure 8: Schematic of the corona ionizer with a needle, designed and made for the experiments

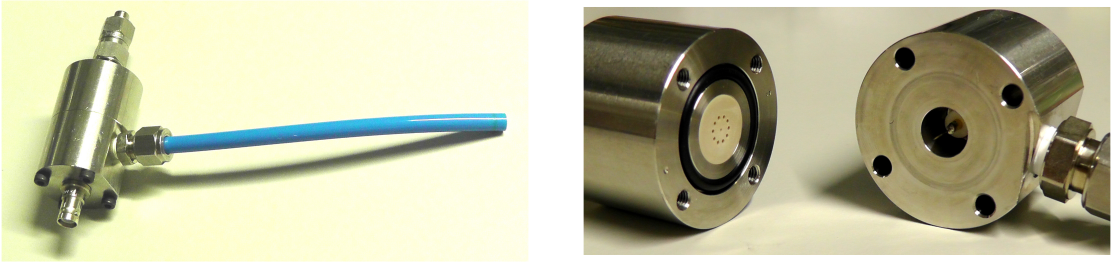

Figure 9: The custom-made corona charger, using an acupuncture needle

Charger Ions

An important aspect when working with aerosol neutralizers is the chemical nature and composition of the produced ions. The neutralization of the aerosol has a direct effect on the chemical composition of the generated molecular clusters. It is crucial to notice that the clusters entering the neutralizer most likely differ in chemical composition from those exiting the device, which are then analyzed, even if only marginally. This is due to the fact that the interaction with ions of unknown chemical species may have an effect on the electrical mobility of the clusters under investigation. The properties of the ions thus depend on the carrier gas conditions and the setup, the used materials as well as their adjustment. Charger ions and their electrical mobility spectra vary with the type of contaminants and impurities in the ambient air (Maißer et al., 2015; Steiner and Reischl, 2012; Steiner et al., 2014; Tigges et al., 2015a).

Steiner et al. (2014) focused on the influence of the carrier gas on the ion production of an ^{241}Am neutralizer. They found that for negative ions the nitrate ion NO_3^- is the dominant species with an electrical mobility $Z = 2.09$ cm^2/Vs.

Maißer et al. (2015) measured masses and mobilities of bipolar ions, generated by a ^{210}Po source, like ^{241}Am an α-emitter. The carrier gas was particle free, dry air. They found that most of the ions originated from components of their experimental setup. Six positive and twenty-five negative ion species were identified. Although the ions originated from materials used for these specific measurements, the authors point out that the ions they found like phthalate, PDMS ions, perfluoroalkanoate ions etc. are typical for this kind of laboratory work as they are part of tubing and sealing materials, and the like (Maißer et al., 2015).

Like Steiner et al. (2014), Maißer et al. (2015) found the nitrate ion to be the most abundant negative ion species.

It may well be assumed that the impurities for the conducted experiments pre-

sented in section 6 are similar to those found by Maißer et al. (2015) and Steiner et al. (2014) due to the similarity of the used materials and instruments.

Figure 10 shows the el. mobility spectra of the three aerosol neutralizers used in the experiments. Figure (a) is the el. mobility spectrum of the positive charger ions generated by the ^{241}Am, and figure (b) the negative charger ions, both at a flow rate of 16 L/min. The solid purple curve in figure (c) depicts the positive charger ions generated by the corona neutralizer at a flow rate of 8 L/min and in figure (d) the dashed purple line indicates the negative charger ions at the same flow rate setting. Figure (e) and (f) are the el. mobility spectra of the positive and negative charger ions generated by the soft X-ray neutralizer at a flow rate of 20 L/min. For the bipolar chargers the ion number concentration [cm^{-3}] of the negative ions is significantly lower than for the positive ions. Only the corona neutralizer produced more negative ions (by a factor of 10). The negative ions have lower inverse el. mobilities than the positive ions, and the peaks of the positive ^{241}Am and corona spectrum are significantly broader than the according negative peaks.

As these electrical mobility spectra were not all measured on the same day, slightly different contaminants and/or impurities influenced the generation of the ions. Figure 10 only presents a qualitative overview as no detailed and thorough analysis of the charger ion species was performed.

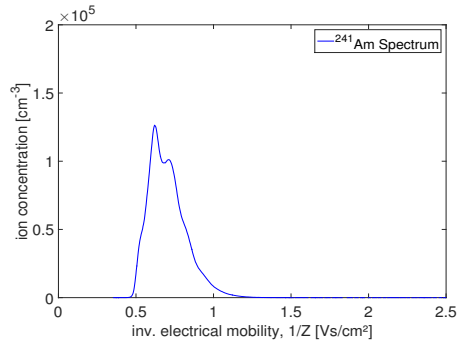

(a) ^{241}Am positive charger ion spectrum

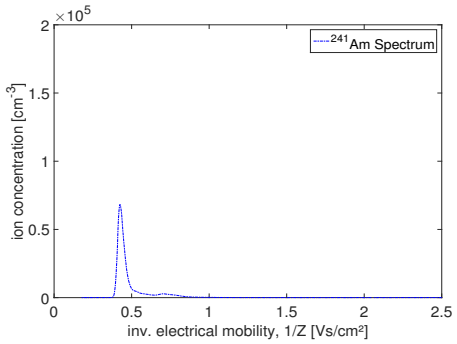

(b) ^{241}Am negative charger ion spectrum

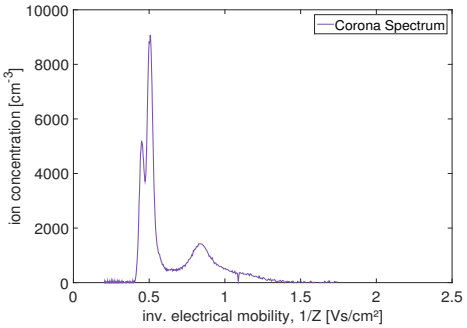

(c) Corona positive charger ion spectrum

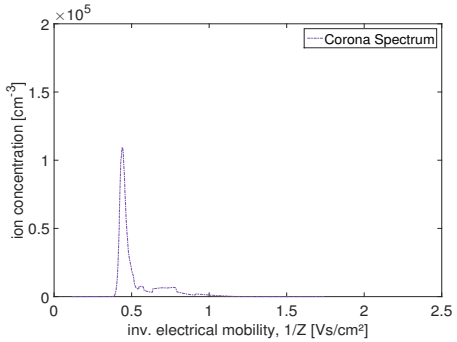

(d) Corona negative charger ion spectrum

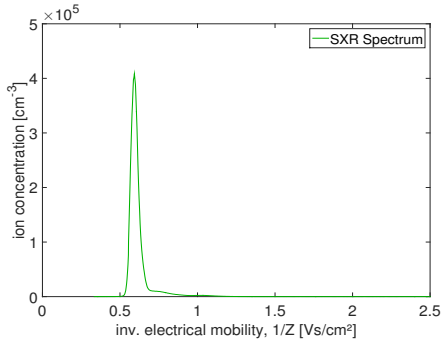

(e) Soft X-ray positive charger ion spectrum

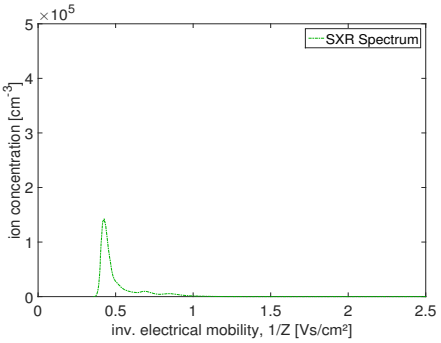

(f) Soft X-ray negative charger ion spectrum

Figure 10: Electrical mobility spectra of charger ions

5.3 Electrostatic classification

Differential **M**obility **A**nalyzer

For the classification of the particles a Vienna type medium flow, high resolution differential mobility analyzer (DMA) was used. "Electrical mobility analyzers, like the differential mobility analyzer, classify particles according to their electrical mobility"(Seinfeld and Pandis, 2006, 431).

Initially, the DMA was introduced as a means of instrument calibration by providing monodisperse aerosol fractions, thus particles of one size. Liu and Pui (1974) and Knutson and Whitby (1975) acted as pioneers and had already realized the potential of the DMA, namely the classification and measurement of size distributions. After improvements in the area of particle detection, the combination between DMA and detector became a powerful tool for determining particle size distributions (Baron and Willeke, 2001). DMAs are applicable to a wide size range, from 1 nm to 1 μm, but are crucial for the size range between 3 and 100 nm particles (Flagan, 1998; Stolzenburg and McMurry, 2008; Winklmayr et al., 1991).

If an electrostatic field is established between two differently charged electrodes, a force acts on charged particles. The strength of the force is directly proportional to the amount of charges the particle carries, see equation (20) in section 4.2. The electrodes can be parallel plates or concentric cylinders.
The relationship between electrostatic field, electrical mobility, terminal electrostatic velocity and particle diameter is given by equation (23). For monodisperse particles, the more charges a particle carries the higher its electrical mobility, see equation (24).

In figure 11 a simple electrical mobility analyzer is shown. The aerosol enters the device on the left side at the center of the two parallel plates. A flow of clean air shields it from the charged plates, which are held at a constant voltage. There are essentially three possible scenarios: First, if a particle is uncharged it passes the device undisturbed, as it is not affected by the electrostatic field. Second, for a given voltage, particles with higher mobilities experience a stronger deflection than particles with lower mobilities, therefore do not reach the exit and adhere to the plates. Third, particles with the matching mobility and below will migrate all the way through the device and can be sampled. By comparing the samples collected at different voltage configurations, it is possible to determine size fractions (Hinds, 1999).

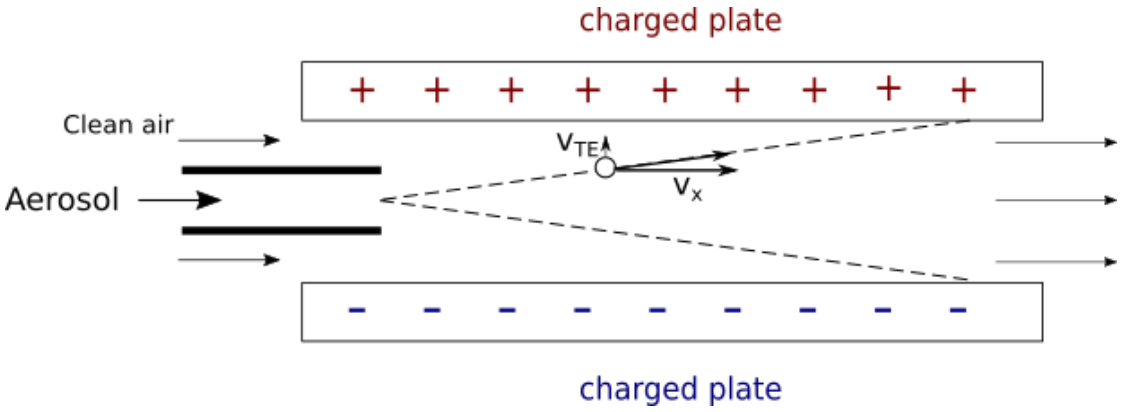

Figure 11: Recreation of a figure in Hinds (1999, 341), depicting a simple electrical mobility analyzer

The working principle of a differential mobility analyzer is basically the same, though especially geometrical considerations are more sophisticated. In the fine and ultrafine regime ($D_p < 20$ nm), the diffusivity of particles is the major limiting factor, whereas for larger particles it is their high inertia. Research efforts for the last 30 years are more concerned with particle sizes smaller than 10 nm, which is also true for this particular thesis. Therefore only problems arising from working

with ultrafine particles are taken into account at this point. The geometry of the DMA has to be adapted, when working within this size range. In order to avoid excessive diffusion losses, it is necessary to reduce the path the aerosol has to travel within the device, which is the channel length. Additionally, the overall flow rate through the device has to be higher than for larger particles to realize high concentrations. Both measures lead to a shorter residence time of the aerosol particles within the DMA, which is favorable for this size range (Winklmayr et al., 1991).

Even though DMAs with radial designs exist as well, only those built like cylindrical capacitors are considered here. Flagan (1998) e.g. provides a very detailed overview of the different types of DMAs and their development.
The electric field within a cylindrical DMA, see equation (39), establishes as a voltage is applied to the center rod, whereas the outer electrode is grounded. It is dependent on the voltage V and the geometrical parameters R_1 - the radius of the inner electrode, R_2 - the radius of the outer electrode, and r - the radial distance from the central axis of the cylinder.

$$E = \frac{V}{r \cdot ln\frac{R_2}{R_1}} \tag{39}$$

The cylindrical geometry of the DMA leads to a flow pattern with cylindrical symmetry which implies that the drift velocity of the particles are solely dependent on r.

The DMA selects particles/clusters of a certain electrical mobility according to the voltage applied to the center rod. Equation (40) shows the relation between the electrical mobility, the geometric and the flow parameters for the Vienna type Differential Mobility Analyzer, a cylindrical DMA developed and introduced by Winklmayr et al. (1991) and Reischl et al. (1997) in the early 1990s.

As shown in figure 12, the particle-free sheath air flow Q_{sh} enters on the left

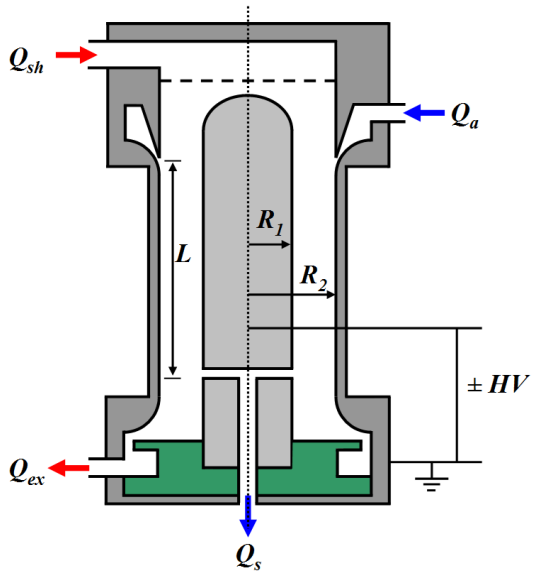

Figure 12: Vienna type DMA, (Steiner, 2011, 31)

side at the top of the DMA. Its purpose is to shield the aerosol particle flow Q_a from the inner electrode, where the voltage V is applied to. The aerosol flow inlet is positioned on the right side. In order to function properly, the flow profile within the DMA has to be laminar. Any turbulences would distort the measurement results. For each voltage setting only particles with the according electrical mobility are sampled and leave the device via the sample flow Q_s outlet, and can be fed to a counting device like an aerosol electrometer or a CPC. Particles with higher mobilities deposit on the inner electrode above the sample excess outlet. Particles with lower mobilities either deposit further downstream or leave the DMA via the excess air Q_{ex} outlet (Baron and Willeke, 2001; Flagan, 1999).

$$Z = \frac{1}{V} \cdot \frac{ln(R_2/R_1)}{2 \cdot \pi \cdot L} \cdot \frac{(Q_{sh} + Q_{ex})}{2} = \frac{ln(R_2/R_1)(Q_{sh} + Q_{ex})}{4\pi V L} \tag{40}$$

R_1 denotes the radius of the inner electrode, R_2 the radius of the outer electrode and L the channel length, all geometrical values. V refers to the potential difference between the inner and the outer electrode, Q_{sh} being the sheath air and Q_{ex} the

excess air.

In order to measure very small particles/clusters within the nanometer range high resolution medium/high flow DMAs are used to minimize diffusion broadening, where the ratio $\frac{L}{R_2-R_1}$ of the geometrical dimensions as well as the sheath air flow rate Q_{sh} are the crucial parameters (Steiner et al., 2010).

Resolution & Diffusion Broadening

The measure of resolution and therefore performance of a DMA is the full width at half maximum (FWHH) of the transfer function.

Knutson and Whitby (1975) define the transfer function, denoted Ω in this notation, as

"Ω = *the probability that an aerosol particle which enters the mobility analyzer via the aerosol inlet will leave via the sampling flow, given that its mobility is* Z_p."(Knutson and Whitby, 1975, 447)

Z_p is the particle electrical mobility, which is denoted as Z in this thesis. Stolzenburg and McMurry (2008) further point out that "it is the probability of the particle, starting at the aerosol entrance of the classification zone, reaching the aerosol exit. Losses in the inlet and outlet zones outside the classification zone are not included in Ω."(Stolzenburg and McMurry, 2008, 422)

Particle diffusion leads to a broadening of the transfer function. The full width at half maximum (FWHH) of the transfer function represents the resolving power of the DMA.

For an ideal DMA without particle diffusion and symmetrical flow conditions ($Q_a = Q_s$, $Q_{sh} = Q_{ex}$), the shape of the transfer function as an isosceles triangle, depicted in figure 13, and the relation given in equation (41) holds.

$$\frac{\Delta Z}{Z} = \frac{Q_a}{Q_{sh}} \tag{41}$$

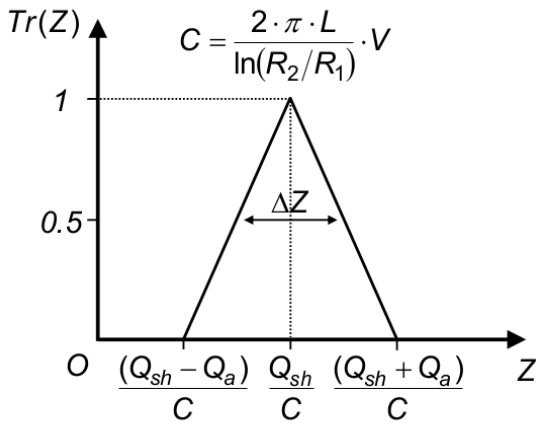

Figure 13: Transfer function for an ideal DMA and symmetrical flow conditions (Steiner et al., 2010, 312).

The resolution R for an ideal DMA and non-diffusive particles is given in equation (42),

$$R = \frac{Z_p^*}{\Delta Z} \tag{42}$$

where Z_p^* denotes the characteristic mobility at a given flow rate and voltage setting and ΔZ the full width at half maximum (FWHH) of the transfer function (Baron and Willeke, 2001).

If particles are diffusive and/or the flow pattern is not perfectly laminar, the shape is distorted towards a more Gaussian shape, hence a broadening of the transfer function (Stolzenburg and McMurry, 2008; Reischl, 1991).
The main reasons for this broadening are therefore due to DMA geometry and operating conditions (Steiner et al., 2010).

UDMA

The UDMA, a high resolution, medium flow Vienna type DMA was introduced by Steiner et al. (2010). It is a further development of the original Vienna type

DMA with the form of a vertical cylindrical capacitor. To summarize, the main differences to the predecessors are: a redesign of the terminal port of the high voltage power supply and the exit section. In order to reduce weight many parts are made of aluminium.

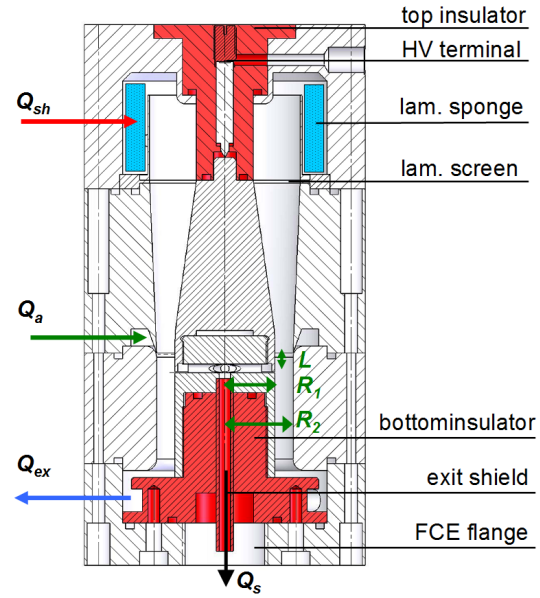

Figure 14: Vienna type UDMA (Steiner, 2011, 59)

The Vienna Type UDMA as shown in figure 14 consists of a top insulator (made of polyetherethertekone PEEK), a HV terminal, a laminarization sponge and screen, a sheath air inlet, an aerosol inlet, a bottom insulator (made of PEEK), an exit shield, an excess air outlet and a FCE flange. Flow port tube joints are manufactured of stainless steel.

The channel length and width are 6.50 mm. The sheath air flow range lies between Q_{sh} = 400 - 700 L/min. The radius of the inner electrode R_1 = 17.5 mm and of the outer electrode R_2 = 24 mm.

Sheath air Q_{sh} inlet and excess air Q_{ex} outlet are mounted to the DMA by a KF 25 flange, which feeds sheath air and removes excess air via one manifold and six

radial inlet and outlet ports.

Laminarization sponge and screen ensure a laminar Q_{sh} flow profile within the UDMA. The aerosol flow Q_a also enters the UDMA tangentially and mixes with the sheath air flow. Appropriate design implementations were chosen to avoid turbulences in the area where the two flows merge. The aerosol sample flow Q_s exits the device via the exit slit, a narrow circular aperture situated in the center rod. The UDMA runs in a closed loop arrangement with $Q_{sh} = Q_{ex}$ and $Q_a = Q_s$. Closed loop arrangements are common when working at high sheath air flow rates. For this operation mode equation (40) reduces to equation (43). The voltage on the center rod can be varied between 1 V and 10 kV for both polarities.

$$Z = \frac{Q_{sh}}{2\pi LV} \cdot ln(\frac{R_2}{R_1}) \tag{43}$$

The calibration of the UDMA prior to each measurement, presented in section 6, is done by determining the operational characterization factor K given by equation (44).

$$K = \frac{ln(\frac{R_2}{R_1})}{2\pi L} \cdot Q_{sh} \tag{44}$$

Even without knowing the exact geometric parameters and the sheath air flow rate, which is especially difficult for the high flow regime, K "can be determined experimentally by feeding aerosol particles with a well known electrical mobility to the DMA and recording the voltage where most of the particles are transferred from Q_a to Q_s"(Steiner et al., 2010, 311).

"The resolution of the differential mobility analyzer (DMA) is conveniently described as the ratio of the mobility at the peak of the column transfer function to the full width of the transfer function at $\frac{1}{2}$ of its maximum value."(Flagan, 1999, 556) According to this definition the resolution R of the UDMA for $D_p = 1.47$ nm is 30 (Steiner et al., 2014).

From electrical mobility to electrical equivalent diameter

There are different possibilities and procedures to invert the particle electrical mobility Z into the according electrical mobility equivalent diameter d_Z. One being the 'Millikan-Fuchs' relationship only considering spherical particles. This relationship is based on equation (23) derived from Stokes law (15) including the slip correction given by equation (45), which includes slightly different constants than the slip correction stated in equation (16).

$$C_C(D_p) = 1 + \frac{2\lambda}{D_p}[1.246 + 0.420e^{-0.87\frac{D_p}{2\lambda}}] \tag{45}$$

For the size range $0.5nm < D_p < 5nm$, the 'Millikan-Fuchs' relationship can be approximated by the Mäkelä approximation (Mäkelä et al., 1996), see equation (46). Mäkelä et al. (1996) use the name 'Millikan-Fuchs' relationship, because their approximation is based on the form and constants used first by Millikan, and later by Fuchs.

$$Z_p = 2.2458 \times 10^{-22} \cdot D_p^{-1.9956} \tag{46}$$

For reasons of simplicity, the approximation used in this thesis, called 'approxD', to invert electrical mobilities into equivalent diameters is in fact a linearization of the 'Millikan-Fuchs' approximation, see figure 15. It shows that for the size range below 10 nm this approximation (in red) is in very good agreement with the 'Millikan-Fuchs' relationship (in blue). The resulting equivalent diameters are listed in section 7, see tables 9 and 10.

$$D_p \approx \sqrt{2.01 \times \frac{1}{Z}} \tag{47}$$

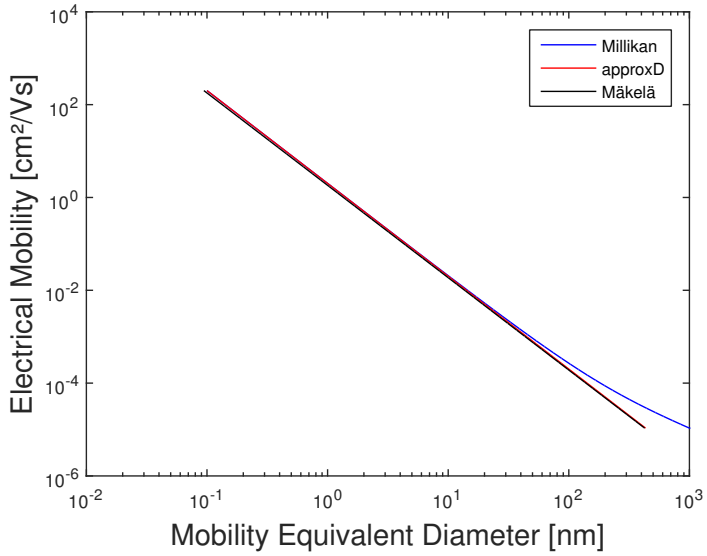

Figure 15: Comparison of the data inversion from electrical mobilities to electrical equivalent diameters: Millikan-Fuchs relationship in blue, Mäkelä approximation in black and the linearization of Mäkelä approximation 'approxD' in red

5.4 Particle Detection

Only after the development of suitable particle detectors, DMAs could also be used to measure aerosol size distributions (Baron and Willeke, 2001).

For these measurements, a Faraday Cup Electrometer was used as a particle detector, where the electrical signal in form of a current reflects on the particle number concentration. The aerosol electrometer consists of an electrometer and a filter inside a Faraday cage. Since the cavity of an electrical conductor is always field-free, incoming charged particles if deposited on the filter cause a compensating current. The current can be measured by an electrometer and converted into a voltage signal. The voltage signal can the be related to the particle concentration (Winklmayr et al., 1991; Willeke and Baron, 1993).

The compensation current (see equation (48)) is equal to the product of sample

flow rate Q_s and the net charge concentration of the particles c_q.

$$I = Q_s c_q \qquad [A] \tag{48}$$

Compared to a CNC/CPC (condensation nuclei/particle counter) the main advantages of this type of detector are the possibility to detect particles/clusters in the molecular size range, the short response time and the favorable behavior concerning diffusion losses (Reischl et al., 1996; Winklmayr et al., 1991). Furthermore, the electrometer and its counting efficiency is not only independent of size, but also of the chemical properties of the particle, unlike the CPC (Winklmayr et al., 1991; Winkler et al., 2008).

Briefly for clarification, condensation particle counters are limited in these previously mentioned regards, because the particles are introduced in a supersaturated environment, then grow via condensational growth to sizes which are detectable by optical means. For very small particles, supersaturation must be very high and also chemical composition plays a significant role (Hinds, 1999; Baron and Willeke, 2001).

The main drawback of using FCEs instead of CPCs is that they have a higher threshold of particle detection, meaning that a minimum particle concentration is needed for proper functioning. In other words, the compensation current must be higher than the electrical noise of the FCE. No calibration of the FCE was performed prior to the experiments as it was used as an absolute measuring method, still keeping in mind that diffusion losses do occur.

6 Experiments

This work aims at providing calibration standards in the size range of 1 to 4 nm. In order to achieve this goal, electrical mobility measurements were conducted using three aerosol neutralizers to determine their applicability as well as eligibility for working with tetra-alkyl ammonium halides. Figure 16 shows the electrical mobility spectrum of THABr for a setup where the electrospray is flanged directly to the UDMA. Beyond 1.5 Vs/cm^2 the spectrum gets distorted by multiply charged clusters. The neutralization of excessive charges to one, enables the resolution of clusters $A^+(AB)_2$, $A^+(AB)_3$, $A^+(AB)_4$ etc. with larger electrical mobility equivalent diameters.

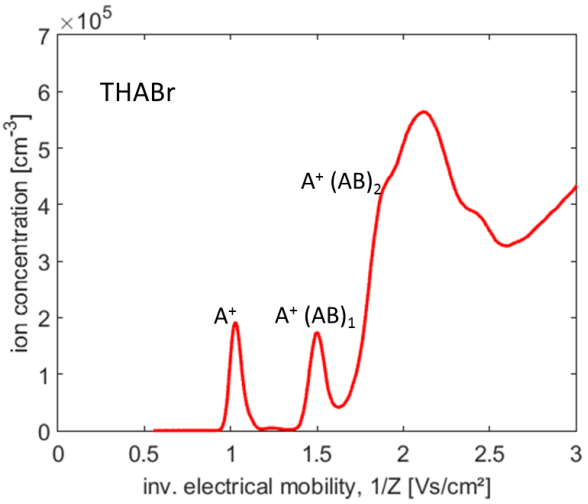

Figure 16: THABr spectrum

For high resolution measurements of nanoparticles using a DMA, it is crucial to guarantee laminar flow conditions. To provide a stable sheath air flow, blower and pump were turned on approximately 30 minutes prior to each experiment.
The UDMA is operated in a closed loop arrangement as described in section 5.3. The voltage range of the scanning mode is always adapted to the working substance and the polarity of the charged clusters. The increment for the scanning

mode is set to $\sqrt[2]{128}$, the measurement period of each voltage step is 0.5 s.
To minimize the risk of deposition at the tip of the capillary, the voltage of the ES is set before applying the pressure control, which was 2-3 kV for most of the experiments. For each setting three runs were recorded to be able to average in a meaningful way.

6.1 Experiment I - ^{241}Am

The first series of electrical mobility measurements are performed using a bipolar ^{241}Am ionizer. Depicted on the left side of figure 17 is the initial setup with a critical orifice of 6.5 L/min, determining the aerosol flow rate Q_a, an applied air flow of approximately 16 L/min through the electrospray generator and an overflow for the excess air, which is led to a gas vent. The setup shown on the right is slightly modified using a 14.44 L/min critical orifice, an aerosol flow of $\sim$ 14 L/min and no overflow.
Particle free compressed air is fed to the electrospray as carrier gas for the molecular clusters, which are then introduced to the ^{241}Am neutralizer. Dependent on the voltage applied to the ES, the positively/negatively charged clusters mix with the bipolar ions before entering the differential mobility analyzer. The function of the neutralizer is to reduce excessive charges of the clusters to (ideally) one. Subsequently, the clusters are classified by the DMA according to their electrical mobility, and finally the aerosol sample flow Q_s is fed to the Faraday cup electrometer, which acts as a particle counter.
The idea behind the second configuration is that the aerosol stream is not pushed into, but rather drawn into the DMA to avoid a potential overpressure in the DMA classification region.
The measurements were conducted for both positive and negative molecular clus-

ters of THABr, TBAI, TPrAI and MTOA-BF3I.

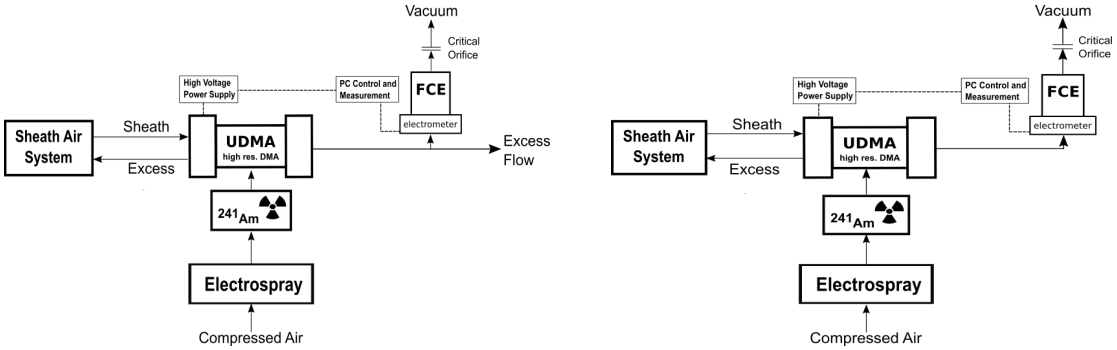

(a) The first experimental setup with the ^{241}Am source and a critical orifice of 6.5 L/min

(b) The second setup without an overflow and a critical orifice of 14.44 L/min

Figure 17: Setup 1

6.2 Experiment II - Soft X-Ray

The experimental approach follows the description in section 6.1. Due to the longer travelling path, the flow through the electrospray was increased to 20 L/min and diluted solutions of the mobility standards were applied to maximize the signal of smaller cluster species, especially monomer and dimer. The critical orifice of 6.5 L/min was used for all measurements.

The advantage of the soft X-ray source is the possibility to turn off the device which enables the measurement of the not neutralized spectrum of each substance and polarity using the same setup as for the experiments with the active neutralizer. Diffusion losses associated with the travelling distance, then occur in both cases to the same extent. This allows the comparison of peak heights and therefore it is possible to roughly estimate the neutralization effect of the device for the high flow rate setting and the test substances.

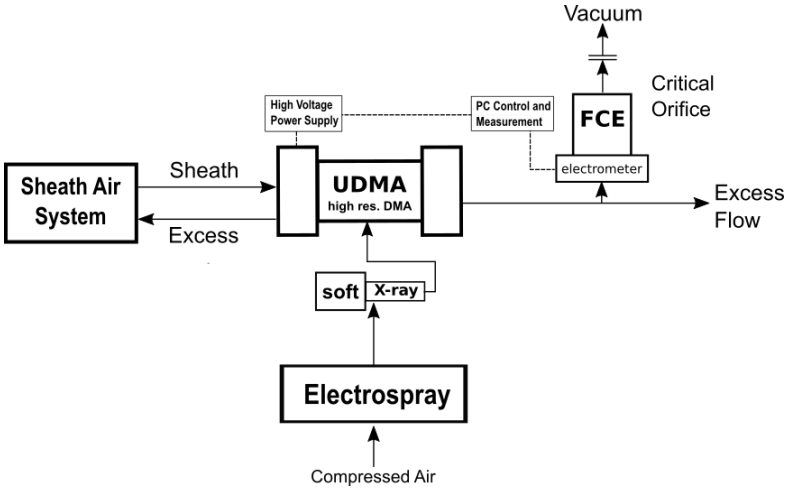

Figure 18: The experimental setup for testing the TSI soft X-ray neutralizer

6.3 Experiment III - Corona

The corona neutralizer required an additional air and voltage supply. Even though flow rates through electrospray and corona were varied, the critical orifice of 6.5 L/min was used for all measurements. There are different possibilities how to operate a corona ionizer. In these experiments the aerosol flow did not pass through the ionizer itself, like in the work done by e.g. Alguacil and Alonso (2006). The ionizer was mounted on top of a T-piece, which connects electrospray and DMA. The ions were pushed down by the air stream to mix with the clusters generated by the electrospray while migrating towards the DMA. Otherwise the setup was very similar to the previous setups shown in figures 17 and 18.
Measurements for two flow configurations were taken, one at $Q{=}\Sigma\ Q_C + Q_{ES} = 16$ L/min, with corona flow $Q_C = 8$ L/min and a flow rate through the electrospray $Q_{ES} = 8$ L/min. The second configuration was with $Q = 12$ L/min, with $Q_C = 7$ L/min and $Q_{ES} = 5$ L/min.

As already mentioned in part 5.2, high ion concentrations are necessary in aerosol neutralization/charging. One limiting factor of a corona ionizers' charging effi-

ciency are deposition losses within the device (Hernandez-Sierra et al., 2003).

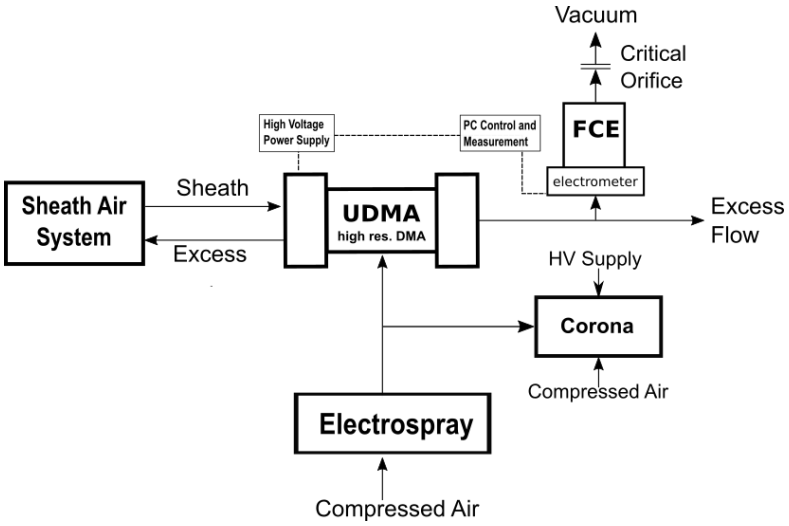

Figure 19: The experimental setup for testing the custom-made corona neutralizer

Since the corona neutralizer was custom-made for this work, a couple of test measurements were performed first. The results are presented at the beginning of section 7 in figures 20, 21 and 22. It shows one series of measurements with different flow rate configurations between Q_C and Q_{ES} and one measurement with a slightly modified setup.

7 Results

In the following section 7, the results of the measurements are presented.
First, general results from measurements of the custom made corona ionizer are shown, see figure 20 & 21. The goal was to map-out the dependency of various flow rates through the corona neutralizer and the ES on the resulting number concentration of the i-mer clusters of THABr.
Figure 22 shows the measurement results with a slightly modified setup 19 including a mixing chamber to increase the residence time t of the electrospray generated clusters and the ions before entering the UDMA.

Second, the main results, showing the positive and negative electrical mobility spectra of each substance with and without one of the three test neutralizers (^{241}Am ionizer, TSI "Advanced Aerosol Neutralizer" and custom-built corona ionizer) are presented in the following way: the figure in the top left corner is the positive or negative spectrum of the substance without an aerosol neutralizer. The spectra are depicted in different shades of red.
The figure in the top right corner shows the spectrum without neutralizer and on top in green - the neutralized spectrum with the soft X-ray neutralizer. The figures in the second row represent the results from the measurements using the radioactive neutralizer; the neutralized spectra are those in blue. On the left hand side, the experimental setup as shown in figure 17 was used. On the right hand side, the setup from figure 18 was used. Differences in aerosol flow conditions are indicated by dashed lines. The spectrum in the bottom left corner is the not neutralized one, and on top the corona neutralized with a flow rate of $Q_C + Q_{ES}$ = 16 L/min in purple. For the neutralized spectrum in the bottom right corner the corona neutralizer was again used, but unlike the spectrum on the left side, a flow $Q_C + Q_{ES}$ of 12 L/min was applied. Again, the difference in aerosol flow

conditions is indicated by the dashed line.

The horizontal axis always shows the inverse electrical mobility $1/Z$ in [Vs/cm^2]. For figures with two overlapping electrical mobility spectra, the left vertical axis shows the ion concentration in [1/cm^3] of the not neutralized curve and the right vertical axis the ion concentration of the neutralized curve. For a better overview, the color of the curve and the according axis is the same. For the most part, the scales of the two vertical axes differ. Each scaling was chosen with the intent of best possible presentation and comparability.

The curves depicted in one plot always represent measurement results from the same day. The plots start with the positive spectra of THABr, followed by negative THABr, then positive MTOA-BF3I, negative MTOA-BF3I, positive TBAI, negative TBAI, positive TPrAI and finally negative TPrAI. The main results are discussed in section 7.1.

The measurement accuracy of the mobility measurements was assumed to be almost exclusively dependent on the stability of the sheath air flow Q_{sh}. The stability was checked for days with long measurement periods, and it was determined that the fluctuations in Q_{sh} are small. They have an impact of less than 1 % on the measured electrical mobility and can therefore be neglected.

Dependency of various flow rates through the corona neutralizer and the ES on the resulting number concentration of i-mer clusters of THABr at $\mathbf{Q_C + Q_{ES} = 12}$ L/min

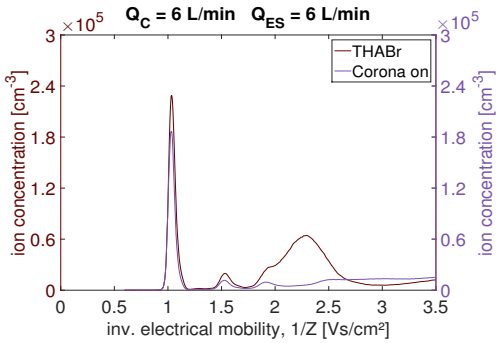

(a) THABr/Corona spectra
Corona flow rate Q_C : 6 L/min
ES flow rate Q_{ES} : 6 L/min

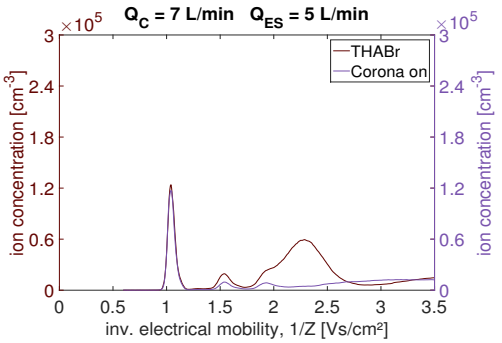

(b) THABr/Corona spectra
Corona flow rate Q_C : 7 L/min
ES flow rate Q_{ES} : 5 L/min

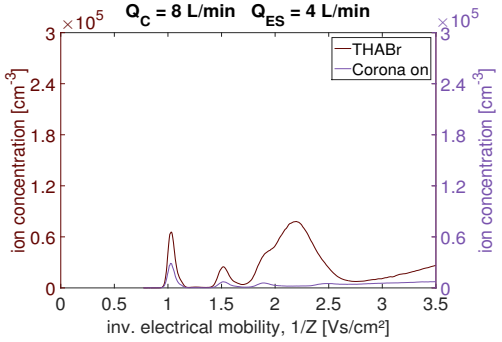

(c) THABr/Corona spectra
Corona flow rate Q_C : 8 L/min
ES flow rate Q_{ES} : 4 L/min

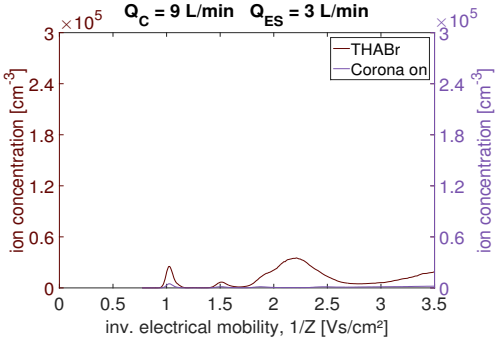

(d) THABr/Corona spectra
Corona flow rate Q_C : 9 L/min
ES flow rate Q_{ES} : 3 L/min

Figure 20: THABr/Corona mobility spectra - Comparison of different flow rate settings with Σ 12 L/min

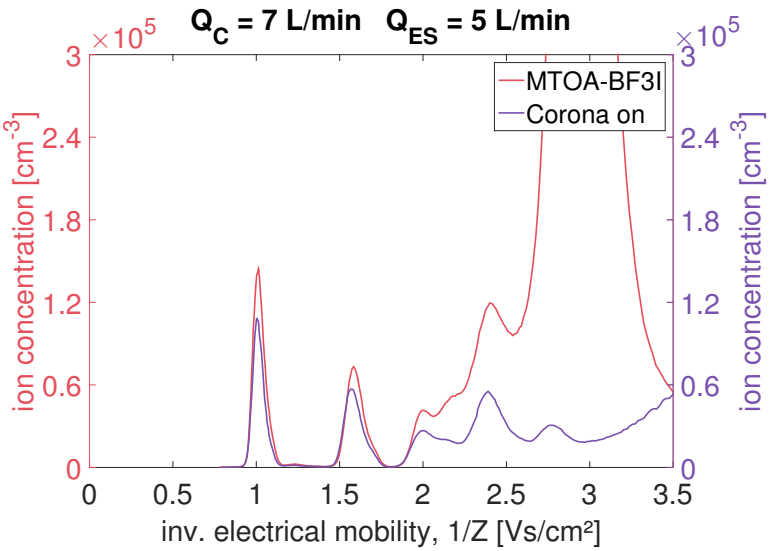

Figure 21: MTOA-BF3I/Corona mobility spectra at $Q_C = 7$ L/min and $Q_{ES} = 5$ L/min

In figure 20 the dark red curves depict the THABr spectra without neutralizer for different flow rates. The number concentration decreases with a decreasing flow Q_{ES}. This behavior can be explained by an increase of diffusion losses due to the low volume flow and the associated longer residence time of the clusters generated by the electrospray. For the purpose of comparability, both the vertical axis on the right side and the left side of the graphs have a maximum value of 2×10^5 cm^{-3} in all figures (a) to (d). The flow rate with $Q_C = 7$ L/min and $Q_{ES} = 5$ L/min was chosen for the main experiments because it also showed good results for MTOA-BF3I, see figure 21. Furthermore it was interesting to have an asymmetric flow configuration.

For the last setting shown in figure 20 (d), the neutralization of the corona is most effective, and the purple spectrum approaches the horizontal axis. That means that almost all positively charged THABr clusters get neutralized by the negative air ions, and are therefore not classified by the DMA. This is because of the high flow rate through the ionizer which causes an enhanced generation of charger ions.

Also, the low ES flow rate settings cause higher diffusion losses of the electrospray generated clusters. This is reflected in the fact that the number concentration is also low for the dark red curve where the corona is inactive.

Figure 22 shows on the left the electrical mobility spectrum of THABr in dark red with the switched-off corona, and in purple with the active corona for the setup in figure 19. The spectra depicted on the right side resulted from a slightly modified setup. A mixing chamber in form of a stainless steel tube with an inner diameter of approximately 4 cm and a length of $\sim$ 7 cm was flanged to the DMA inlet to increase the residence time of the electrospray generated clusters and corona generated ions before entering the UDMA. Since the adaptation did not improve the resolution of the i-mer clusters, and increased diffusion losses, all measurements with the corona ionizer were performed without an additional mixing chamber.

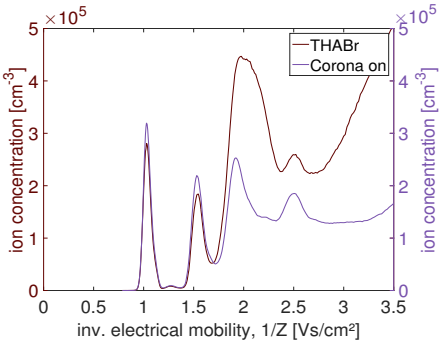

(a) Positive THABr electrical mobility spectrum with and without corona for the setup shown in figure 19

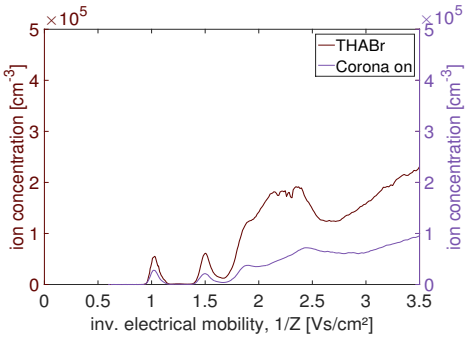

(b) Positive THABr electrical mobility spectrum with and without corona for a modified setup 19 including a mixing chamber

Figure 22

Positive electrical mobility spectra of THABr

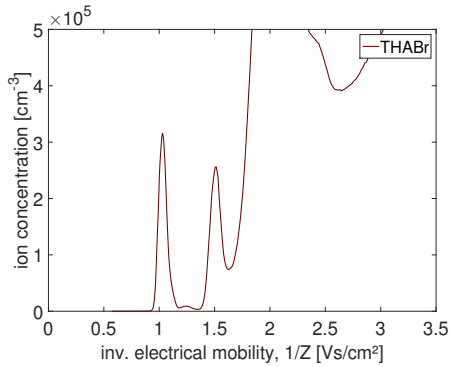

(a) Positive THABr mobility spectrum

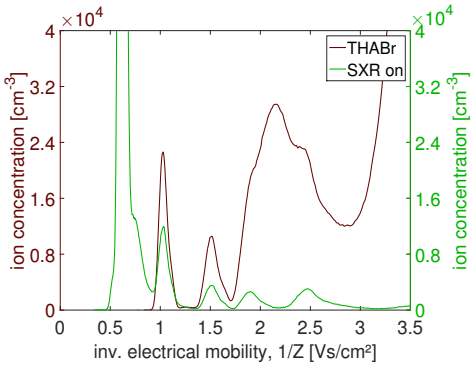

(b) SXR - Q_{ES} = 20 L/min

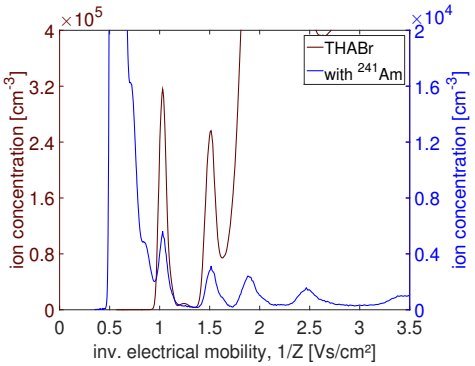

(c) ^{241}Am - Q_{ES} = 16 L/min

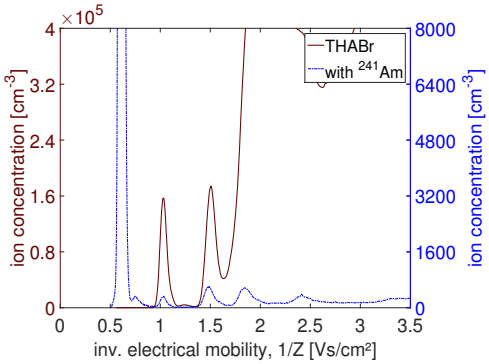

(d) ^{241}Am - $Q_{ES} = Q_a$ = 14 L/min

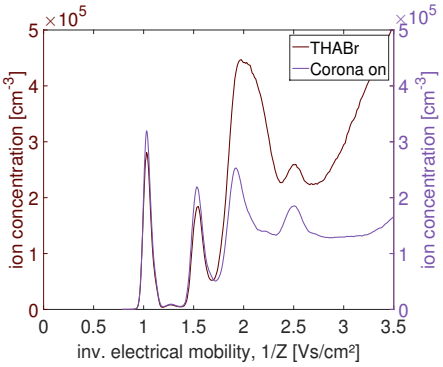

(e) Corona - $Q_{ES} + Q_C$ = 16 L/min

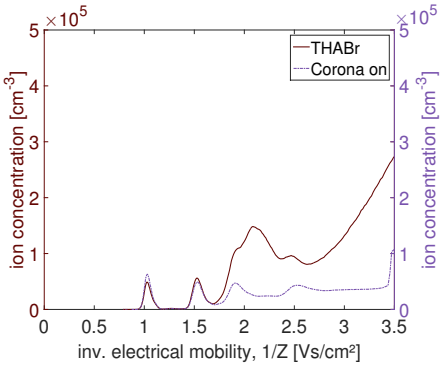

(f) Corona - $Q_{ES} + Q_C$ = 12 L/min

Figure 23: Positive mobility spectra of THABr with three different aerosol neutralizers

Negative electrical mobility spectra of THABr

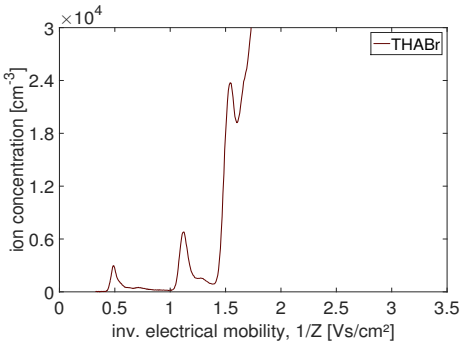

(a) Negative THABr mobility spectrum

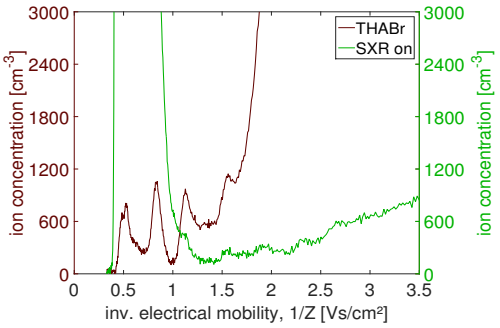

(b) SXR - Q_{ES} = 20 L/min

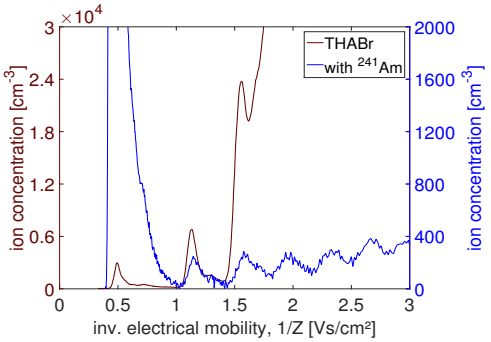

(c) ^{241}Am - Q_{ES} = 16 L/min

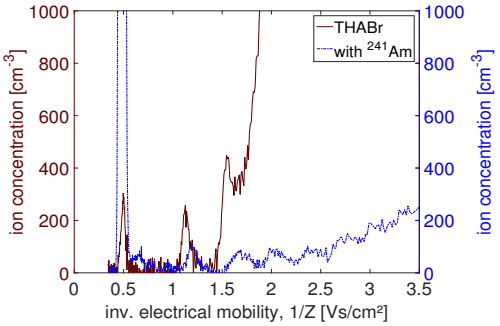

(d) ^{241}Am - $Q_{ES} = Q_a$ = 14 L/min

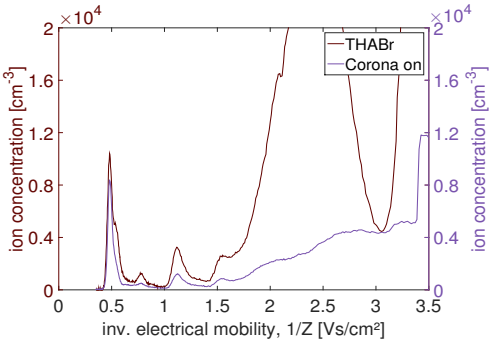

(e) Corona - $Q_{ES} + Q_C$ = 16 L/min

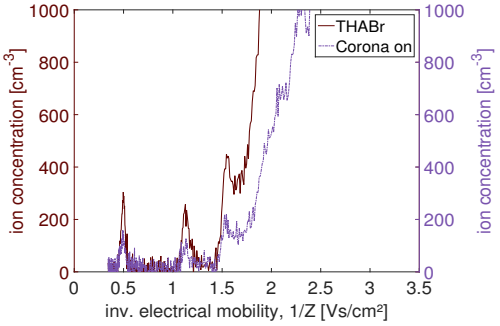

(f) Corona - $Q_{ES} + Q_C$ = 12 L/min

Figure 24: Negative mobility spectra of THABr with three different aerosol neutralizers

Positive electrical mobility spectra of MTOA-BF3I

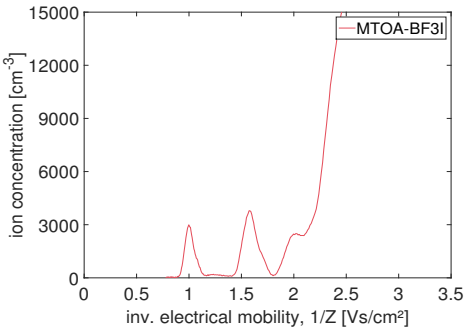

(a) Positive MTOA-BF3I mobility spectrum

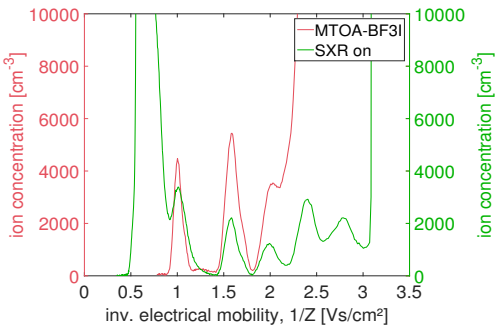

(b) SXR - Q_{ES} = 20 L/min

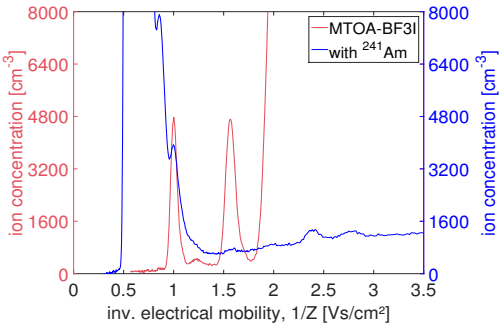

(c) ^{241}Am - Q_{ES} = 16 L/min

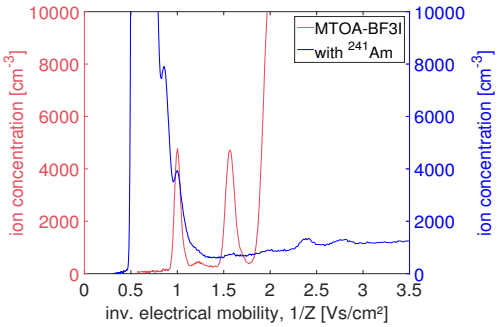

(d) ^{241}Am - $Q_{ES} = Q_a$ = 14 L/min

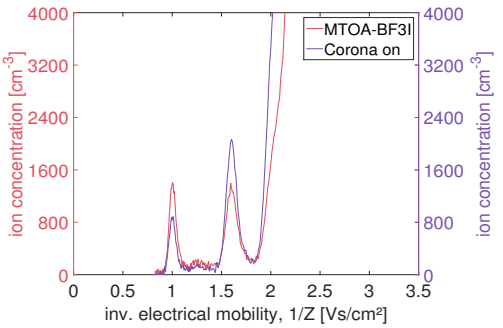

(e) Corona - $Q_{ES} + Q_C$ = 16 L/min

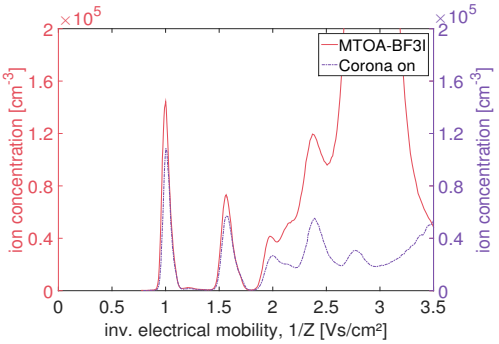

(f) Corona - $Q_{ES} + Q_C$=12 L/min

Figure 25: Positive mobility spectra of MTOA-BF3I with three different aerosol neutralizers

Negative electrical mobility spectra of MTOA-BF3I

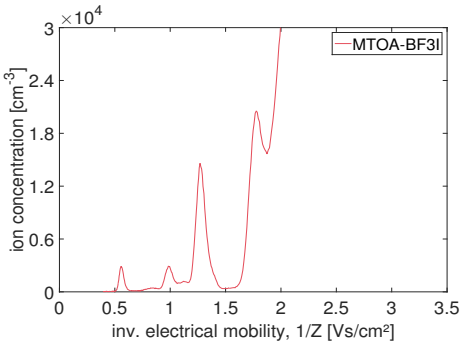

(a) Negative MTOA-BF3I mobility spectrum

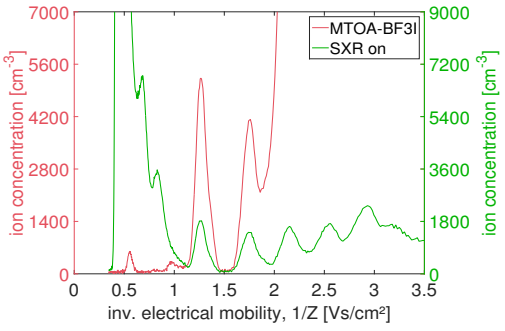

(b) SXR - Q_{ES} = 20 L/min

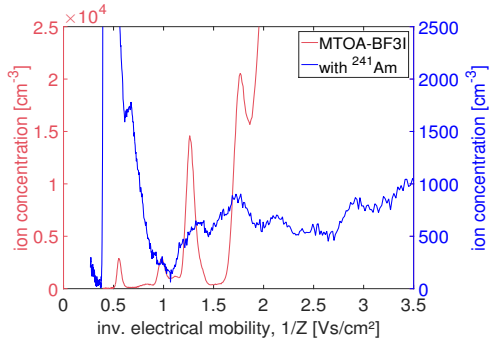

(c) ^{241}Am - Q_{ES} = 16 L/min

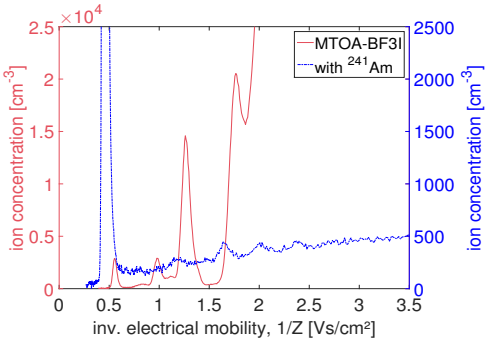

(d) ^{241}Am - $Q_{ES} = Q_a$ = 14 L/min

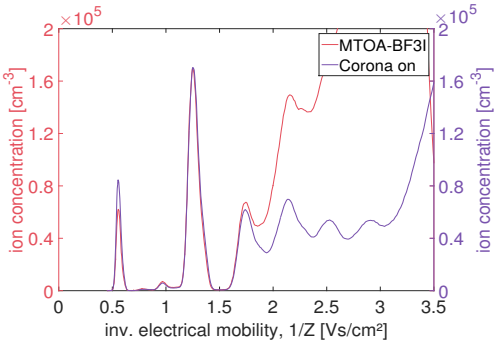

(e) Corona - $Q_{ES} + Q_C$ = 16 L/min

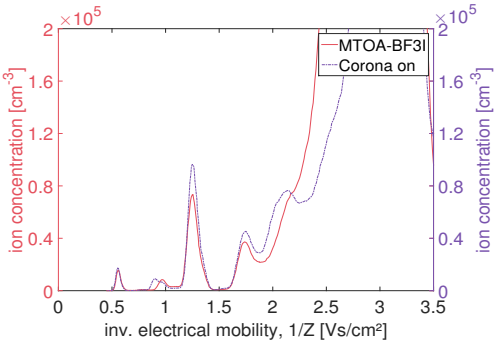

(f) Corona - $Q_{ES} + Q_C$ = 12 L/min

Figure 26: Negative mobility spectra of MTOA-BF3I with three different aerosol neutralizers

Positive electrical mobility spectra of TBAI

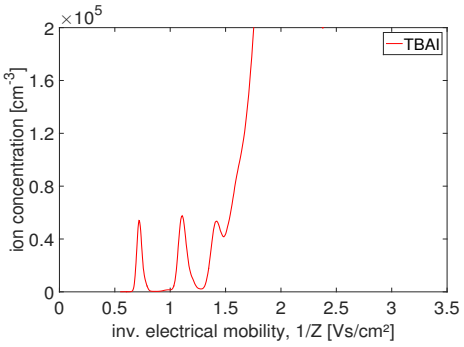

(a) Positive TBAI mobility spectrum

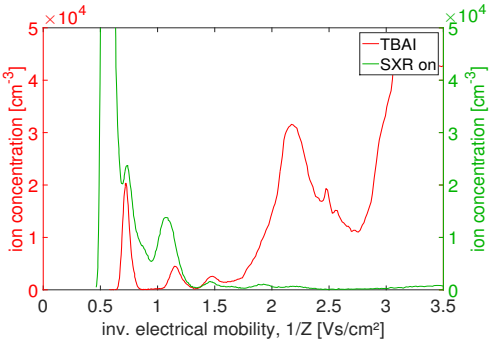

(b) SXR - Q_{ES} = 20 L/min

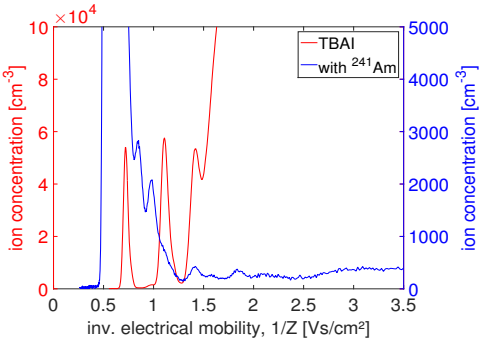

(c) ^{241}Am - Q_{ES} = 16 L/min

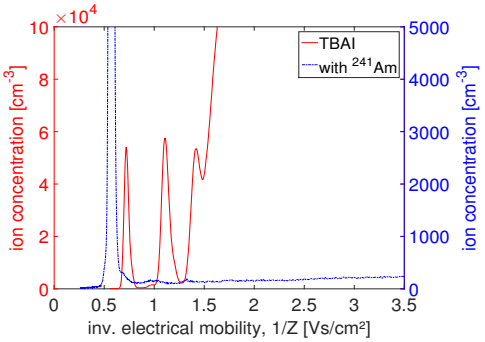

(d) ^{241}Am - $Q_{ES} = Q_a$ = 14 L/min

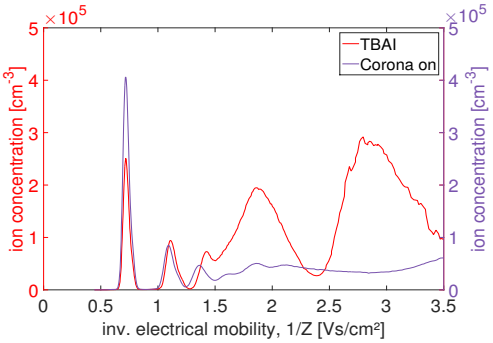

(e) Corona - $Q_{ES} + Q_C$ = 16 L/min

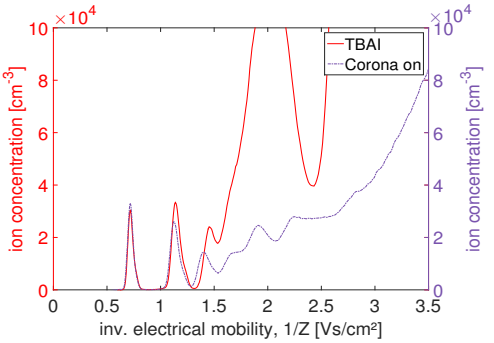

(f) Corona - $Q_{ES} + Q_C$ = 12 L/min

Figure 27: Positive mobility spectra of TBAI with three different aerosol neutralizers

Negative electrical mobility spectra of TBAI

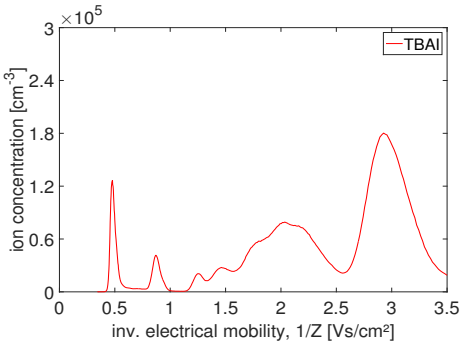

(a) Negative TBAI mobility spectrum

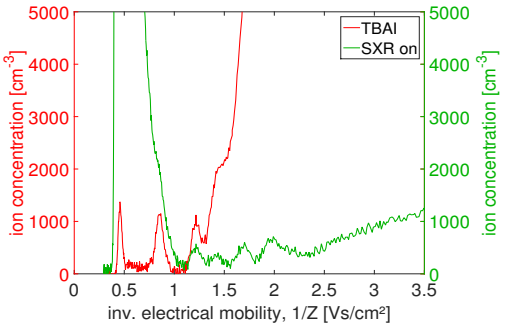

(b) SXR - Q_{ES} = 20 L/min

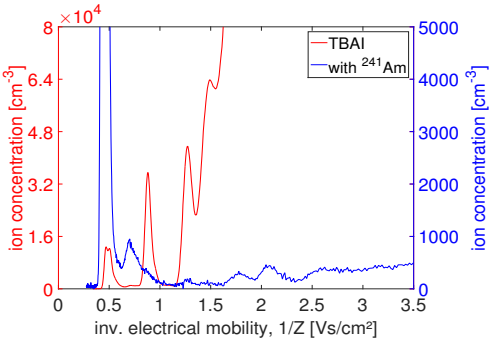

(c) ^{241}Am - Q_{ES} = 16 L/min

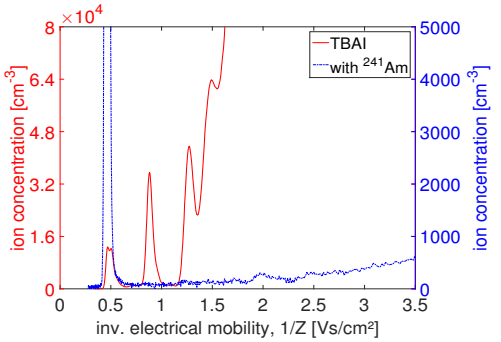

(d) ^{241}Am - $Q_{ES} = Q_a$ = 14 L/min

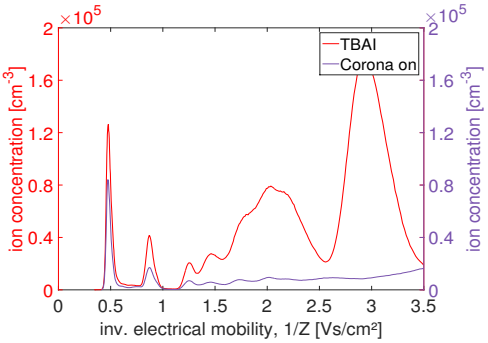

(e) Corona - $Q_{ES} + Q_C$ = 16 L/min

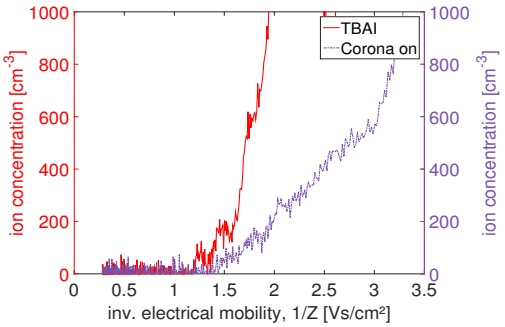

(f) Corona - $Q_{ES} + Q_C$ = 12 L/min

Figure 28: Negative mobility spectra of TBAI with three different aerosol neutralizers

Positive electrical mobility spectra of TPrAI

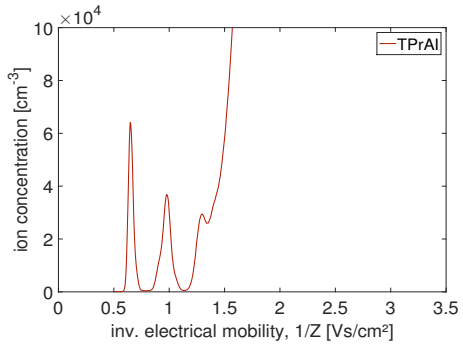

(a) Positive TPrAI mobility spectrum

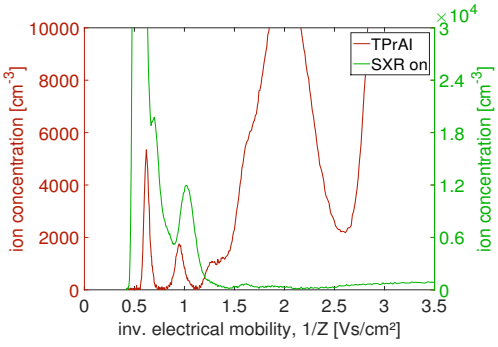

(b) SXR - Q_{ES} = 20 L/min

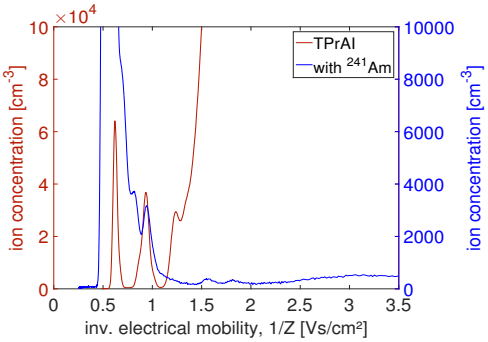

(c) ^{241}Am - Q_{ES} = 16 L/min

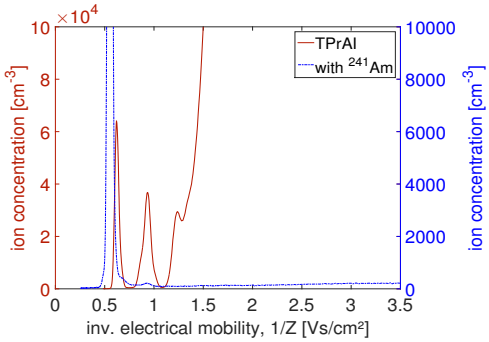

(d) ^{241}Am - $Q_{ES} = Q_a$ = 14 L/min

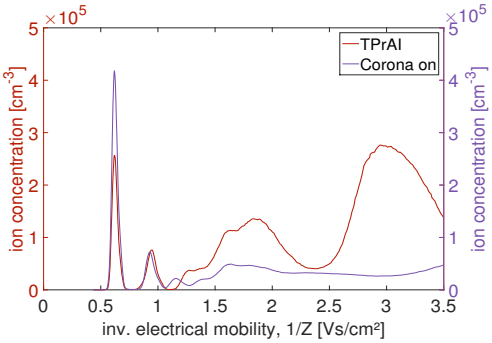

(e) Corona - $Q_{ES} + Q_C$ = 16 L/min

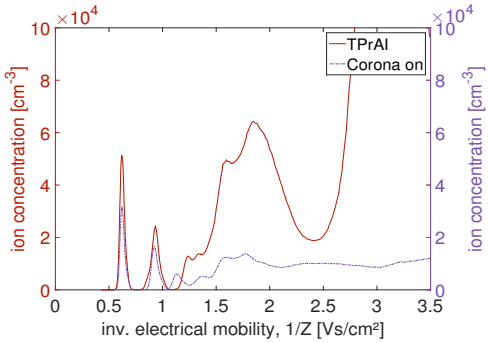

(f) Corona - $Q_{ES} + Q_C$ = 12 L/min

Figure 29: Positive mobility spectra of TPrAI with three different aerosol neutralizers

Negative electrical mobility spectra of TPrAI

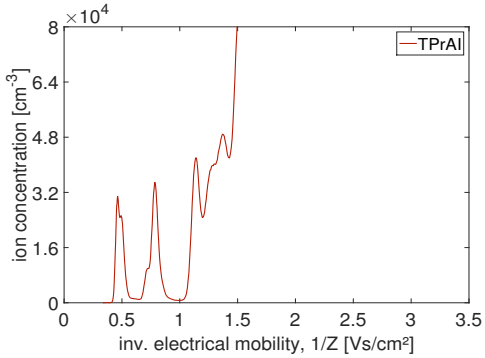

(a) Negative TPrAI mobility spectrum

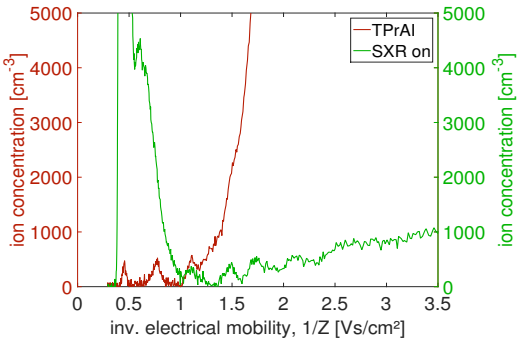

(b) SXR - Q_{ES} = 20 L/min

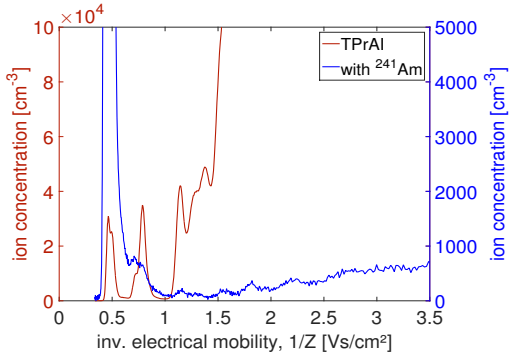

(c) ^{241}Am - Q_{ES} = 16 L/min

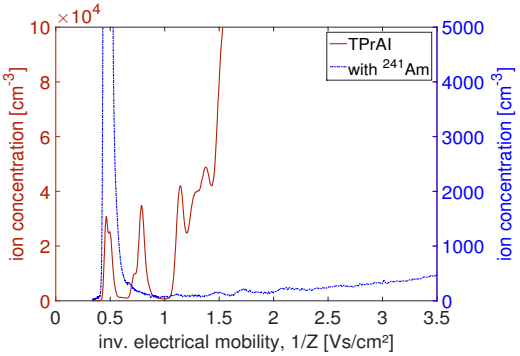

(d) ^{241}Am - $Q_{ES} = Q_a$ = 14 L/min

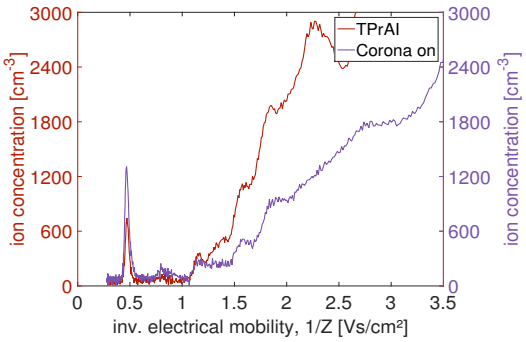

(e) Corona - $Q_{ES} + Q_C$ = 16 L/min

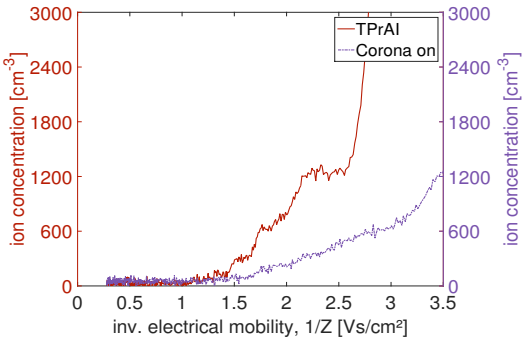

(f) Corona - $Q_{ES} + Q_C$ = 12 L/min

Figure 30: Negative mobility spectra of TPrAI with three different aerosol neutralizers

7.1 Discussion

The use of a neutralizer resulted in the resolution of additional positive THABr cluster peaks for all three test neutralizers shown in figure 23. Especially the soft X-ray and ^{241}Am ionizers neutralized excessive charges of larger clusters very effectively, so that trimer and pentamer are clearly identifiable. However, it was not possible to resolve the tetramer. The different setup and flow conditions for the ^{241}Am neutralizer resulted in a number concentration difference by a factor of 10, see figures 23 (c) & (d). For the different corona flows, the same scale was chosen because the spectrum with $Q = 12$ L/min is still clearly visible. It shows that concentrations decrease with decreasing aerosol flows Q_C and Q_{ES}, which can be expected.

For the negative spectra of THABr, shown in figure 24, the best results were achieved by working at high flow rates through the electrospray ($\sim$ 16 L/min) and short distances.

The spectrum in figure 24 (a) was measured with the electrospray flanged directly to the UDMA. The result depicted in figure 24 (b) can be explained by disturbances on the day of measurement. The dark red curve represents the data obtained with setup 18 and the switched-off soft X-ray source. The second peak is not the dimer of the substance, but either some kind of contamination or fragments of larger i-mers.

The blue solid curve in figure (c) shows the negative THABr spectrum with the ^{241}Am neutralizer at a flow rate through the electrospray of 16 L/min, the aerosol flow Q_a through the DMA was determined by the critical orifice of 6.5 L/min. The excessive flow was led to a gas vent. The use of a neutralizer led to consecutive peaks, even though whether or not they actually correspond to the negative i-mers of THABr cannot be concluded with certainty. The results from the corona

neutralizer shown as the purple curves in figures (e) and (f) show that the i-mers could not have been clearly resolved.

Figure 25 shows the different spectra using MTOA-BF3I. The electrical mobilities of the monomer and the dimer are similar to those of THABr. The monomer A^+ has a mobility close to 1 Vs/cm^2 and the dimer $A^+(AB)_1$ slightly more than 1.5 Vs/cm^2. Resolved peaks of trimer, tetramer and pentamer were obtained by using the soft X-ray and the corona neutralizer. Both results from the ^{241}Am neutralizer do not show clearly resolved peaks unlike the other devices, even though the configuration with $Q_{ES} = Q_a = 14$ L/min worked better than the one with $Q_{ES} = 16$ L/min, depicted in figure (d) of figure 25. The ^{241}Am source seems to neutralize the electrospray generated clusters too effectively.
Figure 25 (e) shows that the corona has no impact on the mobility spectrum. It is possible that the corona did not produce a high enough ion concentration due to contaminations and/or abrasion of the needle. The fact that the peak height of the purple curve exceeds the pink one is probably due to fluctuations in the rate of generated clusters by the electrospray.

For figure 26 (b), unlike the result from THABr, the soft X-ray neutralizer worked astonishingly well. The downside of the device lies in the fact that if one only looks at the neutralized curved, in green, the monomer of the substance is overlapped by the charger peak, as the electrical mobilities of the negative charger ions of the X-ray source cover the range between 0.4 - 1.1 Vs/cm^2. The MTOA-BF3I monomer has an inverse electrical mobility of 0.556 Vs/cm^3 and the dimer approximately 1.27 Vs/cm^2. The small peak between monomer and dimer probably originates from fragments of the dimer or higher i-mers. Again the results using the ^{241}Am neutralizer do not show identifiable cluster species. It seems that

the radioactive source neutralizes the clusters so effectively that only the charger ions are measured by the DMA. The corona yielded determinable i-mers up to almost 3 Vs/cm^2 at a flow rate of $Q_C + Q_{ES} = 16$ L/min depicted in figure 26 (e), even though it failed at fully resolving the peaks.

For TBAI in figure 27, the neutralization effect of the soft X-ray charger in figure (b) seems to be too strong for TBAI. The soft X-ray charger is probably also not a suitable choice when working with TBAI as the electrical mobilities of the charger ions are in the range of the TBAI A^+ (1/Z = 0.718 Vs/cm^2) clusters. Therefore ions of unknown species superimpose the monomer of TBAI. This is also true for the charger ions generated by the ^{241}Am source. Concerning this matter, unipolar neutralization is preferable if also the clusters at the highest mobilities (monomer and dimer) are ought to be measured. The corona spectra are depicted in figures (e) and (f), though the peaks of the cluster i-mers are not fully resolved.

The i-mers of the negatively charged TBAI clusters could not have been resolved by using an aerosol neutralizer, see figure 28. This may be explained by the low flow rate of 12 L/min through corona and electrospray and the low inverse electrical mobilities of the cluster species. The result of the configuration depicted in figure 28 (f) can be traced to complications on the day of measurement.

For TPrAI positive in figure 29, both soft X-ray and ^{241}Am neutralizer are apparently too strong for the purpose. The corona neutralizer works better, but fails to achieve the complete resolution of the peaks.

No meaningful results were obtained for TPrAI negative, depicted in figure 30. For the results in figure 30 (e) & (f), it was very probably due to disturbances on

the day of measurement. The soft X-ray neutralizer is not a suitable instrument when working with clusters with an electrical mobility equivalent diameter of approximately 0.96 nm for the monomer B^-, due to its geometric dimensions. As already discussed, the charger ions of the instrument superimpose monomer and dimer, which as a consequence cannot be resolved.

Figures 23 (e) & (f), 26 (e) & (f), 27 (e) & (f), 29 (e) and 30 (e) show that especially for the monomer of the substances, the purple curve, reflecting on the use of the coroner ionizer, exceeds the one obtained from the data without a neutralizer. Due to neutralization effects, the particle number concentration should be higher for measurements without a neutralizing device, which is true for the majority of the results. This can be most likely explained by instabilities of the ion generation by the electrospray.

Tables 9 and 10 show the measured inverse electrical mobilities and the calculated electrical mobility equivalent diameters for all four substances. Table 9 only includes the results from measurements, where the high voltage applied to the liquid test substances was positive, table 10 includes the ones where negatively charged clusters were generated by the electrospray. Only peaks and their according inverse mobilities, which could be designated with sufficiently high enough confidence to a cluster species, were considered. The values of the positively charged clusters are compared to those of Ude and Fernández de la Mora (2005, 1230). Values obtained from measurements without neutralization were favored over those obtained from measurements with neutralizer, as the tetra-alkyl ammonium halide/ ionic liquid clusters do not mix with ions from unknown species which might influence their electrical mobility. Electrical mobilities for clusters only visible when working with an aerosol neutralizer have the same color as the

neutralized curves in section 7 to indicate the neutralizer used to acquire the value.

Different values for the electrical mobility equivalent diameter between the measured results stated in tables 9 and 10 and those provided by Ude and Fernández de la Mora (2005) are due to different mobility to diameter inversions. The electrical mobilities of THABr cluster species are in quite good agreement with a maximum deviation of 1.48 %. The ideal way to determine the exact electrical mobility would have been to fit the peaks by a Gaussian curve and retrieve the maximum value which corresponds to the electrical mobility of the cluster species in question. This was not done here, therefore the values should be interpreted as very close approximations rather than absolute values.
The measurement results for TPrAI deviate rather strongly from the literature values by more than 7 %. The deviation of TBAI cluster mobilities from the values measured by Ude and Fernández de la Mora (2005) amounts to 3.8 % for the dimer and 2.5 % for the trimer. Unlike THABr and MTOA-BF3I, TBAI and TPrAI measurement results varied significantly with different pressure and voltage settings. Even though the dilution of the substances in acetonitrile were performed with utmost care, the possibility remains that the substances were contaminated, leading to different electrical mobilities of the cluster species. It is also possible that fragmented cluster species were measured and not the actual intact i-mers. Measurements with a mass spectrometer would be necessary to find out the actual reason.

Peak A^+	**THABr**				**TBAI**				**TPrAI**				**MTOA -BF3I**	
	1/Z	D_p	$1/Z_{Ude}$	$D_{p,Ude}$	1/Z	D_p	$1/Z_{Ude}$	$D_{p,Ude}$	1/Z	D_p	$1/Z_{Ude}$	$D_{p,Ude}$	1/Z	D_p
$(AB)_0$	1.03	1.44	1.03	1.47	0.718	1.198	0.718	1.24	0.619	1.115	0.619	1.16	1.002	1.419
$(AB)_1$	1.514	1.74	1.529	1.78	1.109	1.489	1.153	1.55	0.9332	1.37	1.006	1.45	1.571	1.777
$(AB)_2$	1.891	1.95	1.893	1.97	1.414	1.686	1.450	1.73	1.238	1.577	1.338	1.66	1.976	1.993
$(AB)_3$	-	-	2.231	2.14	-	-	1.650	1.84	-	-	1.468	1.74	2.373	2.184
$(AB)_4$	2.466	2.226	2.486	2.26	-	-	1.906	1.98	-	-	1.684	1.86	2.769	2.359
$(AB)_5$	-	-	-	-	-	-	-	-	-	-	1.949	2.00	-	-

Table 9: This table summarizes the data, obtained by the experiments, where positively charged clusters were generated by the electrospray. The values should be interpreted as reference points, rather than absolute values. The inverse electrical mobilities 1/Z are all given in [Vs/cm^2] and particle diameters D_p in [nm]. All values $1/Z_{Ude}$ and $D_{p,Ude}$ are taken from Ude and Fernández de la Mora (2005, 1230).

Peak B^-	**THABr**		**TBAI**		**TPrAI**		**MTOA -BF3I**	
	1/Z	D_p	1/Z	D_p	1/Z	D_p	1/Z	D_p
$(AB)_0$	0.495	0.998	0.477	0.979	0.4599	0.962	0.556	1.058
$(AB)_1$	1.131	1.508	0.872	1.32	0.779	1.251	1.268	1.598
$(AB)_2$	1.557	1.774	1.252	1.586	1.131	1.508	1.775	1.889
$(AB)_3$	-	-	1.459	1.717	1.367	1.654	2.165	2.086
$(AB)_4$	-	-	-	-	-	-	2.559	2.268
$(AB)_5$	-	-	-	-	-	-	2.947	2.434

Table 10: This table summarizes the data, obtained by the experiments, where negatively charged clusters were generated by the electrospray. The values should be interpreted as reference points, rather than absolute values. The inverse electrical mobilities 1/Z are all given in [Vs/cm^2] and particle diameters D_p in [nm].

8 Conclusion & Outlook

The goal of this work was to reduce excessive charges of larger molecular clusters by using an aerosol neutralizer in order to resolve higher TAAH i-mers up to ideally 3-4 nm. It was achieved to approach this objective by realizing unambiguously identifiable cluster species with a diameter of approximately 2.4 nm. The applicability of three neutralizers for this size range was compared, and a corona ionizer was designed and built for this purpose.

First, the electrical mobility spectra of both positively and negatively charged THABr, MTOA-BF3I, TBAI and TPrAI clusters using a ^{241}Am ionizer were measured. For this first measurement series two different setups, depicted in figure 17, were used. Second, the electrical mobility spectra using the TSI "Advanced Aerosol Neutralizer" Model 3087 were measured, see setup figure 18. Third, the electrical mobility spectra using the newly built corona ionizer were measured, see setup in figure 19. Two flow rate configurations were chosen: 1) 16 L/min with 8 L/min through the corona ionizer mixing with 8 L/min through the electrospray and 2) 12 L/min with 7 L/min through the corona ionizer and 5 L/min through the electrospray.
Additional measurements with different flow rate settings were performed and presented in figure 20 and 21.

The measurement results show that whether or not it is possible to resolve the i-mers depends on the substance and the size of the clusters. For small clusters the geometry of the neutralizer plays an important role as diffusion losses increase. Furthermore, it could be shown that for small cluster species it is preferable to work with a unipolar ionizer as the charger ions of the bipolar ionizers have electrical mobilities in the range of the TBAI and TPrAI monomer A^+ and the monomer

B^- of all four test substances.
Additionally, a corona has the advantage that it makes it possible to influence the ion production rate by regulating the applied voltage. Theoretically, excessive neutralization effects can thus be avoided.

This thesis leaves various points for further investigation. The charging efficiency of the corona ionizer was not thoroughly analyzed, due to the more qualitative nature of the experiments. Moreover, there were some challenges with the corona. The ion generation was not always stable, and the necessary voltage to cause the electrical breakdown and a high enough ion generation rate changed between measurements. It would be of interest to perform measurements with different needles to know whether or not these inconsistencies are related to the material and type. Also, the wear of the needle tip caused by the applied high voltage is a possible reason for the reduced functioning.
Due to the number of different substances and setups, it was not possible to optimize all the parameters that influence the measurement like pressure settings, high voltage applied to the test substance, flow conditions and dilution, prior to each measurement.

Despite the previously mentioned points, the main shortcoming of the presented experiments lies in the fact that the used aerosol neutralizers generate ions of unknown species which then attach to the clusters and therefore 'contaminate' them. Meaning that after the neutralizer, the clusters are not the pure species generated previously by the electrospray. This problem was elegantly solved by Férnandez de la Mora and Barrios-Collado (2017), using two electrosprays of opposite polarity with the same species in order to reduce the charges. It yielded remarkable results, realizing sharp mobility peaks up to extremely high orders.

References

Alguacil, F. J.; Alonso, M. 2006. Multiple charging of ultrafine particles in a corona charger. Journal of Aerosol Science, 37(7), 875–884.

Alonso, M.; Martin, M.; Alguacil, F. 2006. The measurement of charging efficiencies and losses of aerosol nanoparticles in a corona charger. Journal of Electrostatics, 64(3), 203–214.

Baron, P.; Willeke, K. 2001. Aerosol measurement: principles, techniques, and applications. A Wiley-Interscience publication. Wiley, 2nd edition.

Cooper, D. W.; Reist, P. C. 1973. Neutralizing charged aerosols with radioactive sources. Journal of Colloid and Interface Science, 45(1), 17–26.

Férnandez de la Mora, J.; Barrios-Collado, C. 2017. A bipolar electrospray source of singly charged salt clusters of precisely controlled composition. Aerosol Science and Technology, 51(6), 778–786.

Flagan, R. C. 1998. History of Electrical Aerosol Measurements. Aerosol Science and Technology, 28(4), 301–380.

Flagan, R. C. 1999. On Differential Mobility Analyzer Resolution. Aerosol Science and Technology, 30(6), 556–570.

Fuchs, N. A. 1963. On the stationary charge distribution on aerosol particles in a bipolar ionic atmosphere. Geofisica pura e applicata, 56(1), 185–193.

Gamero-Castaño, M.; Fernández de la Mora, J. 2000. Direct measurement of ion evaporation kinetics from electrified liquid surfaces. The Journal of Chemical Physics, 113(2), 815–832.

Hernandez-Sierra, A.; Alguacil, F.; Alonso, M. 2003. Unipolar charging of nanometer aerosol particles in a corona ionizer. Journal of Aerosol Science, 34(6), 733–745.

Hinds, W. 1999. Aerosol technology: properties, behavior, and measurement of airborne particles. Wiley-Interscience. Wiley, 2nd edition.

Hoppel, W. A.; Frick, G. M. 1986. Ion—Aerosol Attachment Coefficients and the Steady-State Charge Distribution on Aerosols in a Bipolar Ion Environment. Aerosol Science and Technology, 5(1), 1–21.

Intra, P.; Tippayawong, N. 2009. Progress in unipolar corona discharger designs for airborne particle charging: A literature review. Journal of Electrostatics, 67 (4), 605–615.

Jiang, J.; Attoui, M.; Heim, M.; Brunelli, N. A.; McMurry, P. H.; Kasper, G.; Flagan, R. C.; Giapis, K.; Mouret, G. 2011. Transfer Functions and Penetrations of Five Differential Mobility Analyzers for Sub-2 nm Particle Classification. Aerosol Science and Technology, 45(4), 480–492.

Kallinger, P.; Steiner, G.; Szymanski, W. W. 2012. Characterization of four different bipolar charging devices for nanoparticle charge conditioning. Journal of Nanoparticle Research, (6), 944.

Kilpatrick, W. 1971. An experimental mass-mobility relation for ions in air at atmospheric pressure. Proc.Annu.Conf.Mass.Spectrosc., (19), 320–325.

Knutson, E.; Whitby, K. 1975. Aerosol classification by electric mobility: apparatus, theory, and applications. Journal of Aerosol Science, 6(6), 443–451.

Ku, B. K.; Férnandez de la Mora, J. 2009. Relation between Electrical Mobility,

Mass, and Size for Nanodrops 1–6.5 nm in Diameter in Air. Aerosol Science and Technology, 43(3), 241–249.

Kulkarni, P.; Baron, P.; Willeke, K. 2011. Aerosol Measurement: Principles, Techniques, and Applications. Wiley, 3rd edition.

Liu, B. Y.; Pui, D. Y. 1974. A submicron aerosol standard and the primary, absolute calibration of the condensation nuclei counter. Journal of Colloid and Interface Science, 47(1), 155–171.

Maißer, A.; Thomas, J. M.; Larriba-Andaluz, C.; He, S.; Hogan Jr., C. J. 2015. The mass–mobility distributions of ions produced by a Po-210 source in air. Journal of Aerosol Science, 90, 36–50.

Mäkelä, J.; M.Riihelä; Ukkonen, A.; Jokinen, V.; Keskinen, J. 1996. Comparison of mobility equivalent diameter with Kelvin-Thomson diameter using ion mobility data. J.Chem.Phys., 105(4), 1562–1571.

Reischl, G.; Mäkelä, J.; Karch, R.; Necid, J. 1996. Bipolar charging of ultrafine particles in the size range below 10 nm. Journal of Aerosol Science, 27(6), 931–949. Fuchs Memorial Issue.

Reischl, G. P. 1991. Measurement of Ambient Aerosols by the Differential Mobility Analyzer Method: Concepts and Realization Criteria for the Size Range Between 2 and 500 nm. Aerosol Science and Technology, 14(1), 5–24.

Reischl, G. P.; Mäkelä, J. M.; Necid, J. 1997. Performance of Vienna Type Differential Mobility Analyzer at 1.2–20 Nanometer. Aerosol Science and Technology, 27(6), 651–672.

Rosell-Llompart, J.; Fernández de la Mora, J. 1994. Generation of monodisperse

droplets 0.3 to 4 μm in diameter from electrified cone-jets of highly conducting and viscous liquids. Journal of Aerosol Science, 25(6), 1093–1119.

Seinfeld, J.; Pandis, S. 2006. Atmospheric Chemistry and Physics: From Air Pollution to Climate Change. A Wiley-Interscience publication. Wiley, 2nd edition.

Steiner, G. High Resolution Mobility Spectrometry Of Molecular Ions And Their Effect On The Charging Probabilities of Airborne Particles Under Bipolar Diffusion Charging Conditions. PhD thesis, University of Vienna, 2011.

Steiner, G.; Reischl, G. P. 2012. The effect of carrier gas contaminants on the charging probability of aerosols under bipolar charging conditions. Journal of Aerosol Science, 54, 21–31.

Steiner, G.; Attoui, M.; Wimmer, D.; Reischl, G. P. 2010. A Medium Flow, High-Resolution Vienna DMA Running in Recirculating Mode. Aerosol Science and Technology, 44(4), 308–315.

Steiner, G.; Jokinen, T.; Junninen, H.; Sipilä, M.; Petäjä, T.; Worsnop, D.; Reischl, G. P.; Kulmala, M. 2014. High-Resolution Mobility and Mass Spectrometry of Negative Ions Produced in a 241Am Aerosol Charger. Aerosol Science and Technology, 48(3), 261–270.

Steiner, G.; Franchin, A.; Kangasluoma, J.; Kerminen, V.-M.; Kulmala, M.; Petäjä, T. 2017. Production of neutral molecular clusters by controlled neutralization of mobility standards. Aerosol Science and Technology, pages 1–10.

Stolzenburg, M. R.; McMurry, P. H. 2008. Equations Governing Single and Tandem DMA Configurations and a New Lognormal Approximation to the Transfer Function. Aerosol Science and Technology, 42(6), 421–432.

Taylor, G. 1964. Disintegration of water drops in an electric field. Proceedings of the Royal Society of London A: Mathematical, Physical and Engineering Sciences, 280(1382), 383–397.

Tigges, L.; Jain, A.; Schmid, H.-J. 2015. On the bipolar charge distribution used for mobility particle sizing: Theoretical considerations. Journal of Aerosol Science, 88, 119–134.

Tigges, L.; Wiedensohler, A.; Weinhold, K.; Gandhi, J.; Schmid, H.-J. 2015. Bipolar charge distribution of a soft X-ray diffusion charger. Journal of Aerosol Science, 90(Supplement C), 77–86.

TSI. Advanced Aerosol Neutralizer Model 3087. Neutralize Aerosols Effectively without a Radioactive Source. TSI Incorporated, 2012.

Ude, S.; Fernández de la Mora, J. 2005. Molecular monodisperse mobility and mass standards from electrosprays of tetra-alkyl ammonium halides. Journal of Aerosol Science, 36(10), 1224–1237.

Willeke, K.; Baron, P. 1993. Aerosol Measurement: Principles, Techniques, and Applications. Van Nostrand Reinhold.

Wimmer, D. Generation and Classification of Airborne Molecular Clusters. Master's thesis, University of Vienna, 2008.

Winkler, P. M.; Steiner, G.; A.Vrtala; Vehkamäki, H.; Noppel, M.; Lehtinen, K.; Reischl, G.; Wagner, P.; Kulmala, M. 2008. Heterogeneous Nucleation Experiments Bridging the Scale from Molecular Ion Clusters to Nanoparticles. Science, 319(5868), 1374–1377.

Winklmayr, W.; Reischl, G.; Lindner, A.; Berner, A. 1991. A new electromobility

spectrometer for the measurement of aerosol size distributions in the size range from 1 to 1000 nm. Journal of Aerosol Science, 22(3), 289–296.

List of Figures